Modeling of Burden Distribution in the Blast Furnace

Tamoghna Mitra

Doctor of Technology Thesis

Thermal and Flow Engineering Laboratory
Faculty of Science and Engineering
Åbo Akademi University

Turku/Åbo, Finland 2016.

Modeling of Burden Distribution in the Blast Furnace

Tamoghna Mitra

Doctor of Technology Thesis

Thermal and Flow Engineering Laboratory

Faculty of Science and Engineering

Åbo Akademi University

Turku/Åbo, Finland 2016.

Supervisor

Professor Henrik Saxén

Head of the Laboratory,

Thermal and Flow Engineering laboratory,

Åbo Akademi University, Åbo, Finland.

Reviewer

Dr. Joseph J. Poveromo

President,

RMI Global Consulting, USA.

Opponent and Reviewer

Dr. Paul Zulli

Professorial Fellow,

University of Wollongong, Australia.

ISBN 978-952-12-3419-4

Painosalama Oy

Turku/Äbo, Finland 2016

Preface

This doctoral dissertation is the result of my research work carried out at the Thermal and Flow Engineering Laboratory, Åbo Akademi University, Finland in 2012-2016. I would like to thank the Graduate School of Chemical Engineering, the Academy of Finland, FIMECC and its SIMP and ELEMET programs and Tekes Finland, for providing the financial support to carry out this research. Additionally, this work would not have been possible without the support from the industrial partners including SSAB Europe (Raahe) and LKAB Sweden.

I would like to express my sincere thanks to my supervisor Professor Henrik Saxén whose guidance and encouragement has made this thesis possible. His indefatigable spirit has been a constant motivation for me in tiring times and I will always be grateful to him for making me love my work.

I would like to express my sincere gratitude to all my colleagues at the laboratory who have made my work enjoyable. I would like to thank Professor Ron Zevenhoven, Docent Frank Pettersson and Dr. Mikko Helle for the wonderful discussions and invaluable inputs to my research. I would like to thank Alf Hermanson and Vivéca Sundberg for all the practical help at every stage of my work and my stay in Finland. I will always be grateful to Professor Nirupam Chakraborti for supporting and encouraging me to visit Finland for my Master's programme and thereby making everything else possible. My stay at the laboratory would not have been half as enjoyable without the great coffee breaks and wonderful time spent with my dear colleagues from past and present: Johan, Calle, Martin, Markéta, Ines, Hamid, Inga, Mathias, Lei, Yaowei, Evelina, Alice. A special thanks goes to H-P and Debanga for sharing the office space and laughs.

I would like to thank Professor Tatsuro Ariyama of Tohoku University, Japan, for hosting me at their esteemed laboratory in 2012 in order to study the reduction behavior of pellets. I would like to thank Ueda-san, Kon-san, Kikuchi-san and Natsui-san for making my stay in Japan a great learning experience.

My stay in Finland has been the most memorable because of all my amazing friends in Åbo: Vinay, Rishabh, Rajesh, Megha, Kamesh, Ayush, Bhanu, Pramod, Manju, Susmita, Patrycja and many others. All of you made Åbo a home away from home. A very special thanks goes to Pallavi for always believing that I have what it takes and always being there for me.

I would like to thank my wonderful extended family, my grandmother, my grandfather, my uncles and aunts and my little cousins whose constant love helped me to move ahead in life. Finally, I would like to thank my wonderful parents, Madhumita Mitra and Nibir Kumar Mitra without whose encouragement and inspiration I would not have been able to move ahead in every step that I have taken.

Turku/Åbo, March 2016,
Tamoghna Mitra.

Abstract

The blast furnace is the main ironmaking production unit in the world which converts iron ore with coke and hot blast into liquid iron, hot metal, which is used for steelmaking. The furnace acts as a counter-current reactor charged with layers of raw material of very different gas permeability. The arrangement of these layers, or burden distribution, is the most important factor influencing the gas flow conditions inside the furnace, which dictate the efficiency of the heat transfer and reduction processes. For proper control the furnace operators should know the overall conditions in the furnace and be able to predict how control actions affect the state of the furnace. However, due to high temperatures and pressure, hostile atmosphere and mechanical wear it is very difficult to measure internal variables. Instead, the operators have to rely extensively on measurements obtained at the boundaries of the furnace and make their decisions on the basis of heuristic rules and results from mathematical models. It is particularly difficult to understand the distribution of the burden materials because of the complex behavior of the particulate materials during charging. The aim of this doctoral thesis is to clarify some aspects of burden distribution and to develop tools that can aid the decision-making process in the control of the burden and gas distribution in the blast furnace.

A relatively simple mathematical model was created for simulation of the distribution of the burden material with a bell-less top charging system. The model developed is fast and it can therefore be used by the operators to gain understanding of the formation of layers for different charging programs. The results were verified by findings from charging experiments using a small-scale charging rig at the laboratory.

A basic gas flow model was developed which utilized the results of the burden distribution model to estimate the gas permeability of the upper part of the blast furnace. This combined formulation for gas and burden distribution made it possible to implement a search for the best combination of charging parameters to achieve a target gas temperature distribution. As this mathematical task is discontinuous and non-differentiable, a genetic algorithm was applied to solve the optimization problem. It was demonstrated that the method was able to evolve optimal charging programs that fulfilled the target conditions.

Even though the burden distribution model provides information about the layer structure, it neglects some effects which influence the results, such as mixed layer formation and coke collapse. A more accurate numerical method for studying particle mechanics, the Discrete Element Method (DEM), was used to study some aspects of the charging process more closely. Model charging programs were simulated using DEM and compared with the results from small-scale experiments. The mixed layer was defined and the voidage of mixed layers was estimated. The mixed layer was found to have about 12% less voidage than layers of the individual burden components.

Finally, a model for predicting the extent of coke collapse when heavier pellets are charged over a layer of lighter coke particles was formulated based on slope stability theory, and was used to update the coke layer distribution after charging in the mathematical model. In designing this revision, results from DEM simulations and charging experiments for some charging programs were used. The findings from the coke collapse analysis can be used to design charging programs with more stable coke layers.

Sammanfattning

Masugnen är den huvudsakliga järnframställningsprocessen i världen som konverterar järnmalm med hjälp av koks och varm bläster till råjärn, som används vid stålframställning. Processen fungerar som en enorm motströmsreaktor där man chargerar partikelformiga råmaterial som bildar lager med olika gaspermeabilitet. Fördelningen av dessa lager, den s.k. beskickningsfördelningen, spelar en avgörande roll för gasfördelningen, vilket påverkar såväl värmeöverförings- som reduktionsprocesserna i ugnen. För att kunna reglera processen borde operatörerna känna till ugnens interna tillstånd och även kunna prediktera hur styråtgärderna påverkar processen. Höga temperaturer och högt tryck i kombination med mekaniskt slitage och svåra omständigheter (korrosiv miljö, gaser med explosionsrisk, etc.) gör det mycket svårt att mäta interna variabler i ugnen. Operatörerna måste därför förlita sig på mätningar som finns tillgängliga vid processens ränder och basera sina beslut på processkunskap och resultat från matematiska modeller. Beskickningsfördelningen är speciellt svår att förstå p.g.a. det komplexa beteendet hos partikelformiga råmaterial under chargeringen. Målet med föreliggande doktorsavhandling var att belysa några aspekter av beskickningsfördelningen samt att utveckla matematiska modeller som kan fungera som beslutstöd vid reglering av beskickning- och gasfördelning i masugn.

En relativt förenklad modell utvecklades för simulering av beskickningsfördelningen i en masugn där materialen chargeras med en roterande ränna (end. bell-less top charging). Modellen som utvecklades är snabb och den kan därför användas av operatörerna interaktivt för att få förståelse för hur materiallagren bildas vid chargeringen. Resultaten verifierades genom att jämföra dem med observationer från försök i liten skala med hjälp av en pilotutrustning vid laboratoriet.

Vidare utvecklades för masugnsschaktet en grundläggande gasfördelningsmodell som utnyttjar beskickningsfördelningsmodellens resultat. Den kombinerade modellen gjorde det även möjligt att implementera sökning efter det chargeringsprogram som ger upphov till en önskad gasfördelning. Emedan detta matematiska problem är såväl diskontinuerligt som icke-differentierbart användes en s.k. genetisk algoritm för att lösa optimeringsproblemet. Resultaten visade att sökmetoden gradvis kunde utveckla chargeringsprogram som allt bättre uppfyllde de uppsatta målen.

Fastän beskickningsfördelningsmodellen som utvecklats ger värdefull information om lagerstrukturen kan den inte beskriva vissa komplexa förlopp, såsom uppkomsten av blandade lager samt kollaps av kokslager. En mer sofistikerad numerisk metod för simulering av partikeldynamik, den diskreta element-metoden (eng. Discrete Element Method, DEM), utnyttjades för att i detalj studera förloppen. Några chargeringsprogram simulerades med DEM och resultaten jämfördes med observationer från modellförsök i liten skala. En metod för bestämning av porositeten och omfattningen av blandade lager utvecklades och tillämpades på de studerade chargeringsprogrammen. Blandlagren befanns uppvisa ca 12% lägre porositet än lagren som består av en enda partikeltyp.

Slutligen utvecklades på basis av stabilitetsteori en matematisk modell som uppskattade omfattningen av kollaps av kokslager då (tyngre) pelletar chargeras på ytan. Denna modell, som utvärderades med såväl DEM-simuleringar som småskaleförsök, användes för att uppdatera kokslagrens form i beskickningsfördelningsmodellens resultat. Modellen kan även utnyttjas vid utveckling av chargeringsprogram som leder till stabila kokslager som inte är benägna att kollapsa.

List of Publications

I. Mitra, T. and Saxén, H. (2014). Model for Fast Evaluation of Charging Programs in the Blast Furnace. *Metallurgical and Material Transactions B, 45*(6), 2382-2394.

II. Mitra, T. and Saxén, H. (2015). Evolution of Charging Programs for Achieving Required Gas Temperature Profile in a Blast Furnace. *Materials and Manufacturing Processes, 30*(4), 474-487.

III. Mitra, T. and Saxén, H. (2015). Discrete Element Simulation of Charging program and Mixed Layer Formation in an Ironmaking Blast Furnace. *Journal of Computational Particle Mechanics*, DOI 10.1007/s40571-015-0084-1.

IV. Mitra, T. and Saxén, H. (2016). Investigation of Coke Collapse in the Blast Furnace using Mathematical Modeling and Small Scale Experiments. *ISIJ International, 56*(9).

Contribution of the author

The author of this thesis is the main author of the publications and has developed all the models presented in them. All the simulations in DEM and some of the charging experiments using the scaled model were performed by the author. Most of the charging program experiments were performed by Simon Renlund and Mathias Sundqvist in close coordination with the author. The DEM simulation and the charging experiments for slump tests for determining the particle properties were performed along with Rikio Soda of Tohoku University, Japan.

Related publications

Besides the listed publications, the author of this thesis has participated in various conferences related to the thesis topic. The publications in the conference proceedings or in associated journals are listed below. It also includes a book chapter which discusses the use of different evolutionary algorithms for ironmaking applications.

V. Mitra, T., Saxén, H. and Chakraborti, N. (2016). Evolutionary Algorithms in Ironmaking Applications. In A.M. Gujrathi and B.V. Babu (Eds.), *Evolutionary Computation: Techniques and Applications.* Oakville: Apple Academic Press.

VI. Mitra, T. and Saxén, H. (2015). Simulation of Burden Distribution and Charging in an Ironmaking Blast Furnace. *IFAC-PapersOnLine, 48*(17), 183-188.

VII. Mitra, T. and Saxén, H. (2015). Investigation of Burden Distribution in the Blast Furnace. *Proceedings of the 10th CSM Steel Congress & the 6th Baosteel Biennial Academic Conference*. Shanghai, China.

VIII. Mitra, T., Mondal, D.N., Pettersson, F. and Saxén, H. (2013). Evolution of Charging Programs for Optimal Burden Distribution in the Blast Furnace. *Computer Methods in Material Science, 13*(1), 99-106.

IX. Mitra, T., Kon, T., Natsui, S., Ueda, S. and Saxén, H. (2013). Reduction Behaviour of Iron Ore Pellet in a Non-Uniform Gas Flow Field. *CAMP-ISIJ*. Tokyo, Japan.

X. Mitra, T., Shao, L. and Saxén, H. (2012). Simulation of Burden and Gas Flow charecteristics using a mathematical model of the upper shaft of the Blast Furnace. *ScanMet IV*, 2, 69-77.

XI. Mitra, T., Kinnunen, K. and Saxén, H. (2012). Evaluation of Alternatives to Raise the Blast Temperature at Lean Blast Furnace Top Gas Operation. *AISTech Conference Proceedings*. Atlanta, USA.

XII. Mitra, T., Helle, M., Petersson, F., Saxén, H. and Chakraborti, N. (2011). Multiobjective Optimization of Top Gas Recycling Conditions in the Blast Furnace by Genetic Algorithms. *Materials and Manufacturing Processes, 26*(3), 475-480.

Contents

1. Introduction

The iron and steel industry is one of the key drivers of today's world economy. This industry fueled the industrial revolution in the 19th century and is the backbone of most of the industrial achievements until today. Iron forms about 5.63% of earth's crust [1] and the majority of it is in the form of oxides (mainly hematite, magnetite and hydroxides). Ironmaking refers to a collection of processes for extraction of metallic iron from these oxides and hydroxides, predominantly using a reductant such as carbon monoxide. Metallic iron is relatively soft, so it is often alloyed with other elements, which improves or imparts properties specific for an application. The alloys of iron are known as steel and the process of alloying is known as "steelmaking". An example of a steel alloy is "Hadfield steel" which contains about 13% manganese and is known for high impact strength and abrasion resistance.

The earliest ironmaking dates back to unrecorded history and the actual origin is contested by various civilizations. Primitive ironmaking techniques involved burning of iron ore using wood in a covered oven and subsequently hammering the slag away to obtain pure iron. Subsequently the process was improved and furnaces called "bloomeries" were introduced during the early industrial era [2]. Modern ironmaking techniques have evolved considerably and presently involve very high production rates, a high degree of automation and sophisticated control strategies. The two most important modern routes for ironmaking are the smelting route and the direct reduction (DR) route. In the smelting route, the prepared agglomerate of iron oxide is reduced and melted and then transported to the steelmaking units. On the other hand, in DR routes the reduction of iron oxides takes place at lower temperatures and the raw material is retained in solid form. The end product is called DRI (Directly Reduced Iron) or sponge iron because of its porous nature. DRI is mainly fed, along with steel scrap, into the Electric Arc Furnaces (EAF) for steelmaking. The blast furnace route is the most important smelting technique, which has existed and flourished for about 500 years. Today it accounts for about 70% of the iron used for crude steel production [3], the rest being mainly recycled scrap melted in other units. It has been a very successful process compared to its alternatives for producing liquid iron from ore because of its fuel efficiency, productivity and scalability.

However, even with the increased production efficiency achieved, the steel industry is known to contribute by a large portion (6-7% [4]) of the global anthropogenic greenhouse gas emissions. In a steel plant, the blast furnace (BF) ironmaking unit is a major energy user [5]. To reduce the energy consumption, a better understanding of the flow phenomena and reduction reactions in the blast furnace is needed. This is particularly important for finding novel and more efficient ways of operating the process. However, the complexity of the system has become the main obstacle for further improvement. By the use of mathematical modeling, it is possible to analyze potential improvements of the process and their effect on the overall performance without expensive full-scale tests.

Blast furnace ironmaking is a complicated process due to its sheer size, large throughput and the numerous physical and chemical phenomena that occur simultaneously. Various first principle and data-driven models have been developed to study either parts of the system or the total process. The earliest mathematical models were zero dimensional models which treated the process as an entity. These were followed by models that divided the furnace into zones where different reactions and phenomena take place. The thermal and chemical conditions were then calculated using thermodynamic relations [6]. In order to understand the variation of solid and gas temperatures, and chemical composition, along the height of the furnace, 1D models were introduced [7-9]. These models discretized the furnace vertically into infinitesimal sections. The heat and mass transfer equations and expressions for the rates of chemical reaction are used to calculate the temperature and composition at different vertical points. The concept was later extended to 2D [10-12] and 3D models using Computational Fluid Dynamics (CFD) and related techniques [13, 14]. An accurate gas flow description required a detailed description of the solid conditions inside the furnace. Therefore, techniques such as the Discrete Element Method (DEM), sometimes coupled with CFD for gas flow, have been increasingly used with the focus on the complex interaction of solid, liquid and gas flow in the furnace [13, 15]. As an alternative approach, there are also various data-driven models that use data from an actual blast furnace to predict different variables, such as the hot metal silicon content [16] or top gas CO_2 content [17].

A robust and accurate mathematical model is crucial for understanding the furnace operation, which forms the basis for controlling the process. A model that can be rapidly executed is also useful for searching the right parameters for achieving a particular output condition. Optimization techniques can also be utilized, which systematically change the input variables of the model to find the state where an objective is minimized (or maximized) to achieve certain goals, e.g., minimum production costs or emission rates.

This doctoral work is focused on modeling with the aim to understand some aspects of the complex burden distribution in the blast furnace. Simplified mathematical models and the more complex DEM approach have been used to describe the burden distribution. The findings have been verified by small scale experiments. Theories pertaining to burden descent, mixed layer formation and coke collapse are proposed. One of the models developed was also optimized to meet targets set for the process conditions using a metaheuristic search algorithm, the Genetic Algorithm. The models developed within this research further the understanding of burden distribution in the blast furnace. The tools developed may be used to help the furnace operators take faster and more appropriate decisions concerning actions controlling the burden and gas distribution.

2. Blast furnace Ironmaking

A blast furnace is a vertical counter-current heat exchange and chemical reactor for producing hot metal. Solid iron oxide burden is charged from top along with coke and flux, and as it descends in the furnace it is heated up by the ascending gas and the iron oxides are reduced into hot metal by the reducing gas. Figure 1(a) shows the cross section of a typical blast furnace along with the inputs and outputs.

The blast furnace parts may be classified depending on the shape of the region (Figure 1, a). The upper cylindrical part of the furnace is known as the throat and is protected by refractory brick. Below the throat, there is the region with increasing diameter known as the shaft which extends to a cylindrical section or belly. After the belly, the diameter decreases again in the bosh region, where the blast enters the furnace. The bottommost portion of the furnace is called the hearth where the molten hot metal and the slag accumulate within a coke bed.

The inner volume of the blast furnace is also classified into different zones (Figure 1, b) depending on the physical state of the burden and the chemical reactions occurring. The uppermost part of the furnace constitutes of the lumpy zone, where the burden remains solid. The iron ore, usually charged as haematite (Fe_2O_3) is first converted to magnetite (Fe_3O_4) and eventually to wustite[1] (FeO) by the ascending reducing gas containing carbon monoxide (CO) which produces carbon dioxide (CO_2).

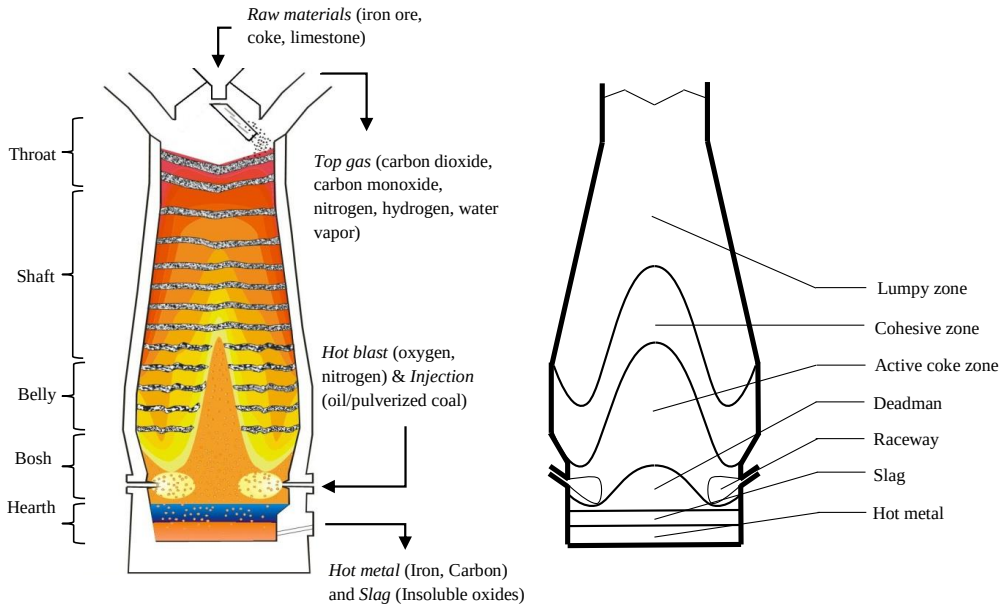

Figure 1: (a) Cross-section of a typical blast furnace, classification based on shape of the furnace region. (b) Different zones of the blast furnace classified on the basis of internal state.

[1] Non-stoichiometric compound, Fe_xO, with a mean value of $x = 0.95$ [18]. For simplicity, wustite is here referred to as FeO.

$$3Fe_2O_3 + CO \rightarrow 2Fe_3O_4 + CO_2 \quad (2.1)$$

$$Fe_3O_4 + CO = 3FeO + CO_2 \quad (2.2)$$

Similar reduction reactions, but to a lesser extent, occur with hydrogen, forming water vapor. The temperature of the burden increases from the ambient to a constant temperature (900 - 1000˚C) where both the burden and the gas attain nearly the same temperature. This region is called the thermal reserve zone. By contrast, the temperature of the gas decreases as it rises in the furnace and exits the top at 100-250 ˚C.

After the end of the thermal reserve zone the wustite is reduced into iron (Fe).

$$FeO + CO = Fe + CO_2 \quad (2.3)$$

A large number of other reactions take place in this region, including reduction of the other metallic oxides in the iron ore and the formation of slag. As some wustite always remains unreduced and the burden reaches higher temperatures than 1000 ˚C, the Boudouard reaction ($C + CO_2 = 2CO$), which is highly endothermic, will occur simultaneously. The net reduction reaction is

$$FeO + C = Fe + CO \quad (2.4)$$

Subsequently, the iron-bearing burden begins to soften and melt as the cohesive zone starts. This zone has alternate layers of highly pervious coke and semi-pervious iron-slag mix. The pervious coke layers or slits help the gas enter from the lower parts of the furnace to rise up towards the top. Therefore, an adequate size of the coke slits is very important for achieving a smooth furnace operation. At the lower end of the cohesive zone, the iron melts and percolates through the bed of solid coke. The upper part of the coke region is called the active coke zone. Here the coke is constantly replenished from the burden, as it slides to the combustion regions near the tuyeres known as the raceways. In the raceway, the coke is combusted to carbon monoxide by the incoming blast which consists of oxygen and (practically inert) nitrogen.

$$2C + O_2 = 2CO \quad (2.5)$$

At the core of the bosh region lies a closely packed column of coke which does not react rapidly and is called the deadman. It provides support to the layered structures above. The hearth has a pool of liquid iron called hot metal with slag floating on top of it. The hot metal and the slag are tapped at regular intervals. The hot metal flows through a runner into a ladle or torpedo, which is transported to the steel mill for further processing. The slag, which is separated by gravity, is usually tapped into a slag pit or directly cooled and granulated. It is often sold as a by-product, e.g. to the cement or brick industries.

In basic terms, the main methods for controlling the conditions inside a blast furnace are by controlling it ‘from below’ through the blast parameters, like temperature, pressure and moisture content, and ‘from above’ by controlling the burden distribution. The latter is the main focus of the present thesis. The next chapter describes the importance of burden distribution and different techniques for controlling it.

3. Burden distribution

The blast furnace is a continuous reactor but the raw materials are charged in alternate layers of ore and coke intermittently. This layered structure is retained as the raw materials descend through the furnace. Burden distribution refers to this arrangement of the layers of different materials inside the furnace and mainly to the radial distribution (as axial symmetry is usually desired). The raw materials charged into the furnace are very different from each other. Ore is about four times heavier than coke and the particle size is 2-4 times smaller, which affects the gas permeability and heating of the charged layers.

As the reducing gas rises from below, it encounters the burden layers with very different permeability conditions. The radial distribution of ore and coke is therefore an important factor governing the gas flow distribution in the furnace [19]. Normally, the fraction of ore of the total volume or mass is used to quantify this distribution. The (radial) region with higher fraction of ore results in a lower gas flow. In some operating procedures, higher gas flow at the center of the furnace is preferred, because it is effective in decreasing discontinuous motion of the solid burden, resulting in smooth operation [20]. Therefore, batches of large-sized coke, known as 'center-coke', or larger sinter and lump ore are charged near the center of the furnace to improve the gas permeability in the region. Only a small number of furnaces are specially equipped to charge coke directly into the furnace center. However, higher gas flow also results in higher gas temperatures as the gas does not have enough time for heat exchange and the thermal flow ratio (defined as the heat capacity ratio between burden and gas) is low. The regions with higher gas temperature usually correspond to a higher cohesive zone level. Therefore, the temperature readings from the above burden probe are an important indicator of burden distribution inside the furnace.

As the burden descends into the furnace, the ore is reduced and at around 1200˚C (depending on the quality of ore), it starts to soften and eventually melts at around 1350˚C. Coke, on the other hand, maintains its form (except some consumption by the solution-loss reaction) until it reaches the tuyere level. The semi-molten portion of the burden is extremely impermeable to the gas flow, so the gas has to flow through more permeable regions, coke slits, in the cohesive zone where it changes to more horizontal direction, until it reaches the lumpy zone. If the coke slits are blocked or not pervious enough, furnace irregularities such as hanging or erratic burden descent may occur. The burden distribution has a major role in affecting the size of coke slits in the cohesive zone, but it also influences the deadman formation in the blast furnace and wear rate of the furnace lining by controlling the gas flow and thus also the heat losses.

Most modern operation practices focus on the growing lack of high-quality raw material and improving the furnace efficiency. These new practices require very precise control of the burden distribution and, therefore, accurate modeling and fast calculations. Thus, simulation of the burden distribution is becoming an increasingly important topic of research. In addition, high coal injection rates through the

tuyeres in blast furnaces reduce the coke rates in the furnace, so the thickness of the coke layers is becoming even less. This requires precise control of raw material distribution to allow sufficient permeability and appropriately located coke slits in the cohesive zone. Some other examples of modern charging practices include mixed charging schemes, where small coke is mixed with ore dumps [21] to improve the permeability of the ore layer. Furnaces around the world are also gradually shifting to high pellet (agglomerated ore) operation owing to its high reducibility, but pellets have lower repose angle, high rolling and layer collapse tendencies [22], so it is very important to understand the layer formation process.

Complex issues associated with burden distribution are coke collapse, segregation and mixed layer formation. These issues have been modeled extensively in the thesis, and in subsequent chapters they will be presented and discussed.

The burden distribution is manipulated by the charging equipment. Modern equipment gives better options for the operator to affect the burden distribution. However, the operator has a limited access to information about the conditions inside the furnace due to extremely high temperatures and the closed nature of the furnace. Therefore, the operators have to rely strongly on existing measurement technologies from where they have to indirectly deduce the conditions inside the furnace. In this chapter, commercially available charging equipment types are discussed along with their differences. Subsequently, some of the measurement technologies employed for understanding the burden distribution conditions are detailed. Finally, the complexity of burden distribution is demonstrated using an example.

3.1 Charging equipment

It is not possible to influence the burden distribution once it has been charged into the furnace as the layers maintain their relative structure quite well until the cohesive zone commences. Burden distribution in blast furnaces is controlled by adjusting the parameters of the charging equipment. Each furnace is charged according to a list, known as ‘charging program’, which consists of the material name, amount and the corresponding set of parameters which determine how the material is to be charged into the furnace. Charging according to this program is repeated over and over during the production process until the program is altered by the operator to accommodate some new situation. Therefore, the layered structure has a repetitive pattern.

There are several available commercial alternatives for blast furnace charging equipment with their own advantages and disadvantages. Some of the common ones are discussed below.

3.1.1 Bell top

A bell top charging system consists of a bell and hopper arrangement. The bell blocks the opening of the hopper when it is raised and when the bell is lowered the raw material falls into the furnace. The hot "top gases" are rich in energy and should therefore be recovered; so a single bell hopper system cannot be used. To avoid loss of the gas, a sealed double bell system is used, as shown in Figure 2.

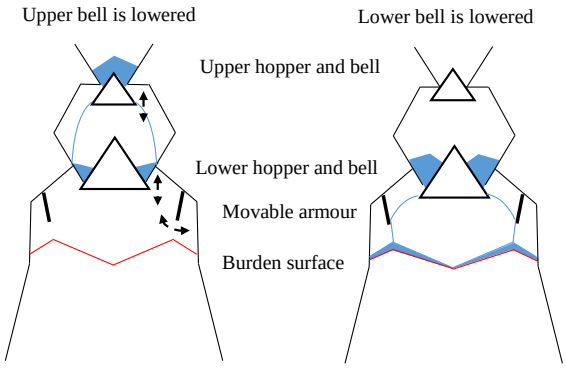

Figure 2: Bell type charging system

Such a charging system is extremely robust but provides very limited flexibility for the operators to design the burden distribution, because there are very few parameters that the operator can influence. Most of the raw material is charged near the wall. Sometimes a set of movable armors, whose position may be set by the operator, is used to redirect the dump away from the furnace walls.

3.1.2 Bell-less top

Bell-less top charging systems (Figure 3) are relatively new charging units which are becoming increasingly popular. This system was developed by Paul Wurth with its first successful industrial application in 1972. It consists of a gated hopper which empties into a chute which is rotating about the axis of symmetry. The inclination of the chute may be controlled and, therefore, provides much higher flexibility to the operator as to choose the size and position of the dump. This is one reason why bell-less charging is preferred over the bell top charging. Yet this charging system has its own limitations; for example, a precise center-coke charge is difficult to achieve, as there is a limitation to how much the chute may be tilted vertically.

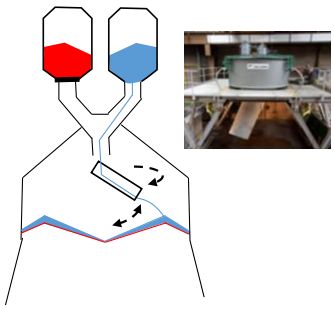

Figure 3: Bell-less top charging system

The bell-less top has helped improve the productivity and coke rate in many furnaces. For example, in an Indian blast furnace equipped with a bell-less charging system the decrease in coke rate exclusively due to improvement of burden distribution was reported to be 10-12 kg/t hot metal [23].

3.1.3 Gimbal top

The Gimbal top (Figure 4) is a comparatively new burden distribution system introduced in 2003 by Siemens VAI [24]. It utilizes a conical distribution chute with rings which allow multi-axis motion. This technology gives more flexibility to the furnace operator compared to the bell-less top charging

system. The charge may be directed to any point on the furnace stock line. It allows sector charging, spot charging and formation of a true center coke charge. This charging system has been applied to a few FINEX and COREX furnaces along with the C Blast Furnace of Tata Steel in Jamshedpur.

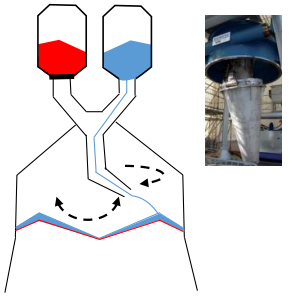

Figure 4: Gimbal type charging system

3.1.4 Bell-less rotary charging unit

A bell-less rotary charging system (Figure 5) was developed by Totem Co. Ltd. [25]. It consists of a rotary chute, whose speed determines the positions at which the material is charged. It charges thin layers of the material, so the dump does not affect the burden surface on which the dump is charged (referred as 'soft dumping'). Some blast furnaces in India have been equipped with this charging system.

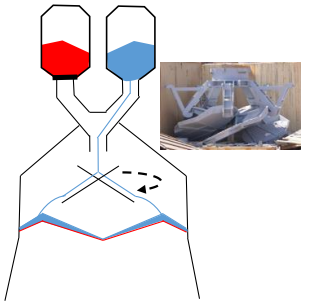

Figure 5: Bell less rotary charging system

3.1.5 No-bell top charging system

The no-bell charging system (Figure 6) was developed by Zimmermann & Jansen Technologies (now IMI Z&J). It consists of a double chute system with a rotating chute at a fixed angle with an additional chute at the end to direct the charge to a particular radial position on the burden surface.

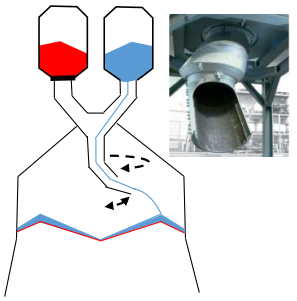

Figure 6: No-bell top charging system

3.2 Measurement technology for blast furnace burden distribution

Efficient blast furnace control requires reliable measurements of the conditions inside the furnace. The temperatures in the lower half of the furnace may increase to more than 2000˚C, where most intrusive measurement technologies would be unreliable, so most of the in-furnace measurements are carried out above or near the burden surface. The most important techniques for direct or indirect quantification of the burden distribution include:

i. Above burden probe

The above burden probe (Figure 7) has a number of thermocouples attached to the device to measure the gas temperatures at different radial positions above the burden

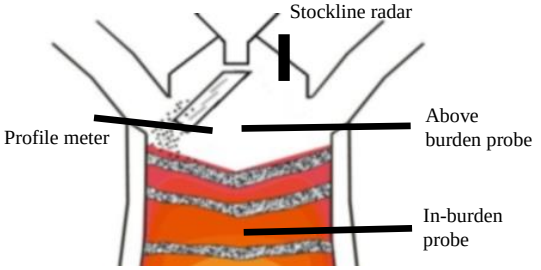

Figure 7: Measurement technology in a typical blast furnace

surface. This provides an idea about the gas flow conditions in the furnace. Figure 8 shows typical gas temperature profiles measured using an above burden probe. The regions with lower permeability allow less gas to flow which reduces the gas temperature compared to regions with higher permeability. Therefore, the temperature readings give an idea about the permeability conditions in the furnace.

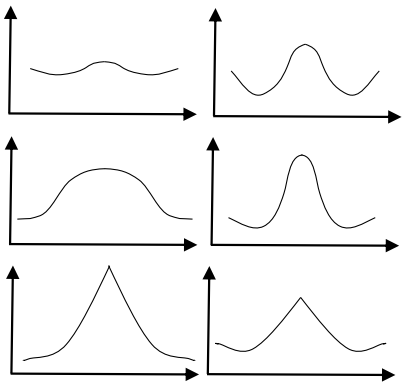

Figure 8: Typical gas temperature distributions measured by above burden probe. Vertical axes shows temperature and the horizontal axes show the distance across the throat diameter.

An issue with the above burden probe is that the gas coming out of the burden surface mixes before it reaches the probe [26]. Therefore, some temperatures may be under- or over-estimated. The probe should thus be mounted closer to the burden surface, which is difficult to realize as the burden surface may vary during the process and with the production rate. Furthermore, a sudden increase in stockline caused by fluidization may destroy the probe.

ii. In-burden probe

In-burden probes (Figure 7) are installed at any height below the burden surface and above the cohesive zone. Therefore, these probes have to survive higher temperature and abrasion compared to the above burden probes. This is the reason why they are usually retractable and only inserted when sampling is done. The probes measure the gas temperature and the composition at different radial points. The measurements are, in general, more accurate than the signals from the above burden probe as mixing does not occur to the same extent. However, strictly speaking, the result will depend on the layer in which the sampling point is at the moment of measuring.

iii. Stockline detector

Stockline detectors (Figure 7) are used to obtain information about the height of the burden surface, known as ‘stockline’, after charging each dump into the furnace. Blast furnaces are programmed so that a dump is charged into the furnace only when the burden surface has descended beyond a certain vertical level. Stockline detectors can be mechanical devices (‘stockrods’) where a weight at the end of a chain or wire is lowered until resistance in the form of burden surface is reached. Modern furnaces use non-contact techniques, such as radar systems which eliminate the time loss while lowering the weight into the furnace. A sudden drop in the stockline is an indication of a slip, which may be a concern for the furnace operator [18].

iv. Profile meter

Profile meters (Figure 7) were originally mechanical devices but today they have been replaced by non-contact methods, e.g., movable radars (moving probe) along a horizontal channel which measure the burden surface height at various radial points. The profile meter can also estimate the burden descent velocity [27]. Modern profile meters have radars fixed on rotary joints and 3D burden surfaces may be estimated, which gives a much better understanding than by measurements along a single direction.

v. Vertical probe

Vertical probes are used to provide the temperature and the gas composition along the height of the furnace. They may consist of cables at different radial positions which are lowered to the burden surface and are dragged down by moving solids until the tip is damaged, as the cables reach high temperatures in the lower part of the furnace. The probes usually measure temperature and pressure and can sample gas for composition. These probes can be equipped with a camera for particle size distribution [28]. The lengths of the eroded probes also indicate the location of the cohesive zone in the furnace. Although vertical probes provide maximum information about the furnace, they are seldom used as they are expensive and require complex feeding equipment.

vi. Thermocouples

Blast furnace walls are lined with thermocouples which also provide crucial information about the furnace operation. For example, sudden changes in thermocouple readings may indicate dropping of skull, which is a stagnant solidified mass formed at furnace walls (Figure 9).

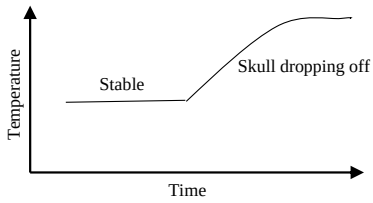

Figure 9: Thermocouple behavior following the removal of skull

vii. Pressure gauges at the furnace wall

Gas pressure is measured at different points on the walls. As the gas flows through the coke slits the direction is horizontal, so it affects the pressure at the walls. Therefore, the pressure information may be used to estimate the cohesive zone shape.

viii. Other measurements

Some of the other measurements from the blast furnace include

1. Pressure, temperature and composition of the top gas
2. Flow rate and rise in temperature of the cooling water
3. Blast conditions
4. Hot metal and slag variables
5. Occasional use of belly probe, tuyere probe, etc.

6. Infrared cameras to measure burden surface temperature
7. Skin flow thermocouples (or mini-probes)

These measurements are indirectly affected by the burden distribution. Using different measurements together with past experience, operators can obtain a holistic view of the conditions in the furnace and identify the cause of improper furnace conditions.

3.3 Complexity of burden distribution

Different charging equipment provide different degrees of control over the charging process, which ultimately determines the burden distribution. Even with a few options, though, the charging process may become very complicated and can be counter-intuitive at times. In this section, this complexity has been analyzed by conducting a sensitivity analysis of the burden distribution to charging parameters for a simulated bell-less top charging system.

A charging program for a bell-less type charging system consists of the material, dump size (mass) and chute angle. It provides reasonable but limited choice to the operator in terms of charging positions on the burden surface. Usually the chute angles are discretized and the operator may select one of the positions. For this exercise a simple reference nine-dump charging program is chosen, as shown in Table 1. Four dumps of coke (C) are charged followed by center coke (CC) and consecutively four dumps of agglomerated ore, or pellet (P), are charged. Chute position 1 indicates that the material is charged near the furnace center, whereas chute position 11 indicates that the material is charged near the wall. In this example, the charging position of each of the coke and pellet dumps varies within the ranges 2-9 and 4-11, respectively, while maintaining the charging positons of the other dumps. The radial distribution of ore-to-coke ratio is calculated using a burden distribution model (described in Sec. 7.2). The results are presented in Figure 10 and are coded as a combination of an alphabet and a number. The alphabet corresponds to the dump number (A is first layer, B is second, etc., cf. Table 1) and the number indicates the charging position of the dump which is altered. It is evident that the burden distribution may be varied considerably by changing the charging position of certain dumps while the results are insensitive to changes in others.

Table 1 Reference charging program for sensitivity analysis.

Layers	1	2	3	4	5	6	7	8	9
Material	C	C	C	C	CC	P	P	P	P
Mass (kg)	1.75	1.75	1.75	1.75	0.40	7.50	7.50	7.50	7.50
Reference chute position	3	4	6	7	1	7	8	10	11
Chute position	2-9	2-9	2-9	2-9	1	4-11	4-11	4-11	4-11
Code	A	B	C	D		E	F	G	H

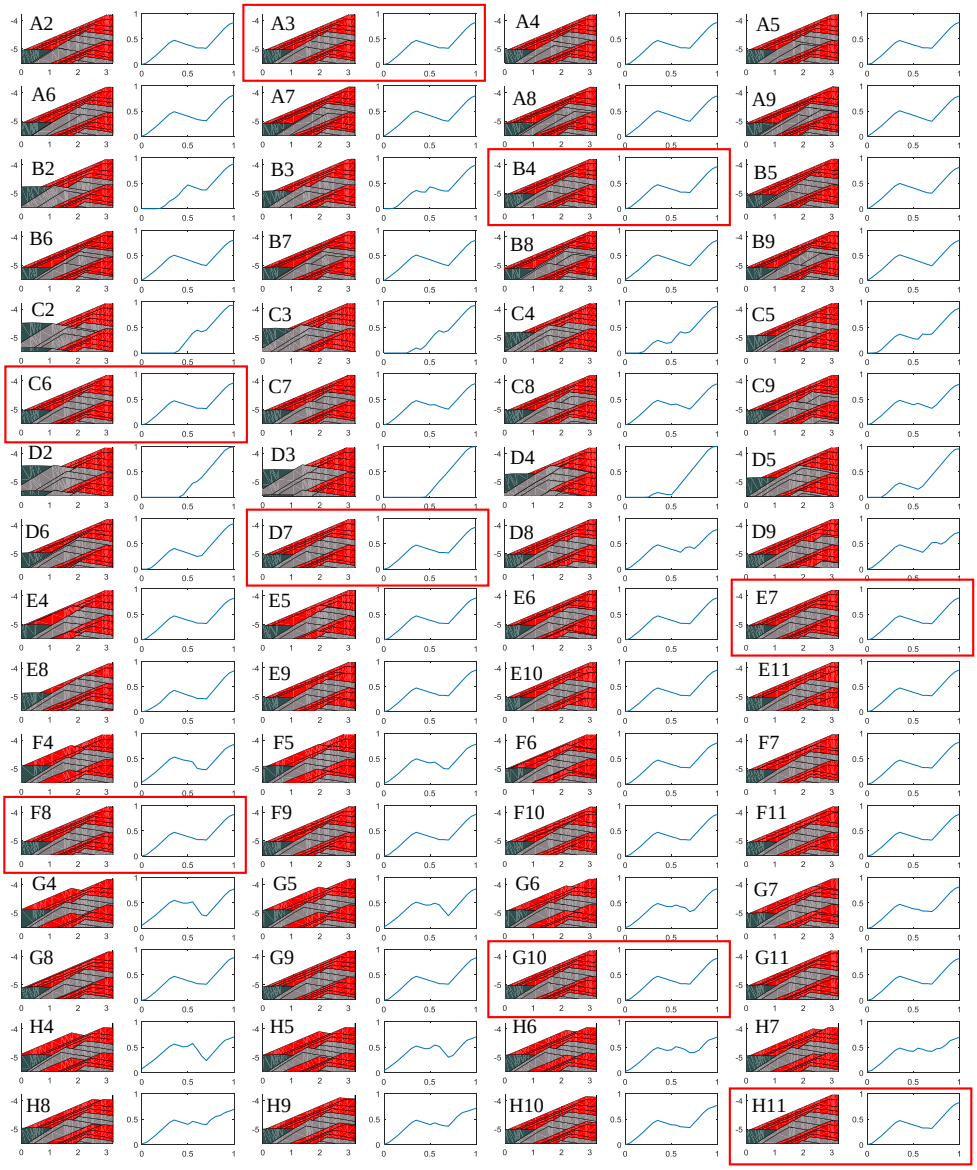

Figure 10: Sensitivity of shifting a layer (dump) in the charging program. The right subpanel for each case shows the radial distribution of the volumetric share of ore in the bed, and the left subpanel the burden distribution. Coke dumps are depicted in grey, center coke in green and pellet in red. Figures enclosed by squares correspond to the profile of the reference program (cf. Table 1).

Figure 11 shows a closer view of the arising burden distribution and the radial distribution of volumetric ore fraction for two of the charging programs in Figure 10, C4 and C5. These charging programs are almost identical, except that the third coke is charged at a difference of one chute position (chute angle difference of 2.4˚). However, the results are quite different: At the intermediate position, the ore fraction is about 10% higher for C5 than for C4, because in C5 the third and the fourth coke dumps create a valley which traps the pellets and prevents them to overflow to the furnace center, as observed in C4. However, such differences do not always arise, as is seen for charging programs A2 and B9: Even though the charging positions of the coke dump are very different (Figure 12), the volumetric distribution of ore is only slightly changed. This is so because the layers together form a very similar coke layer. From these examples it may be concluded that it is very difficult to predict the burden distribution without a mathematical model.

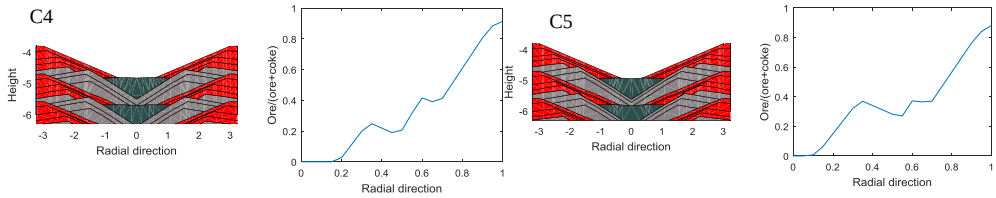

Figure 11: Burden distribution for charging program C4 (left) and C5 (right).

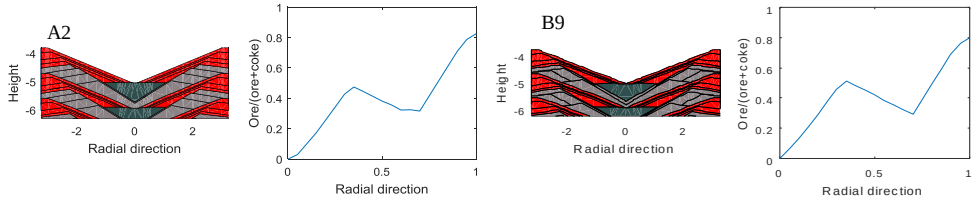

Figure 12: Burden distribution for charging program A2 (left) and B9 (right).

4. Discrete Element Method

Discrete Element Modeling (DEM) is a numerical method for computing the interactions of a large number of solid particles that undergo translational or rotational motion under the influence of external force. DEM is used for simulating the flow and interaction of bulk solids and it has found wide use in studying different phenomena related to particle packing, flow and fluidization [29]. Traditionally, particulate systems have been modeled using continuum methods, similar to the methods used for fluid systems. Unlike fluids, however, particulate systems at rest can transmit shear stress, so additional equations are required to consider this behavior. DEM is a Lagrangian method where the motion of individual particles is simulated explicitly and the bulk behavior is the result of interaction of the particles. DEM also allows for a very detailed study of the interaction of particles, which is not possible in continuum methods.

DEM has been used widely for ironmaking applications for studying the flow of the particles in various stages of material handling and burden distribution inside the blast furnace. It often provides a better insight into the different processes than the continuum techniques.

In DEM, the particles are usually represented by spheres which 'deform' on the application of stress by in contrast to hard spheres in other Lagrangian methods, such as event driven (ED) molecular dynamics. The deformation implies that the particles impinge into each other and the distance between the centers of the spheres is allowed to be less than the sum of their radii. The deformation causes a resistive force in the direction of the collision and the magnitude of the force increases with the extent of deformation.

In this research, DEM was used to study the burden layer formation during the charging process. The simulations were performed using EDEM [30], a commercial software. The fundamental equations used by the software [31] for solution of the different cases are discussed below.

4.1 Fundamental equations

As in any explicit method, the initial position and velocity of each of the particles in the simulation domain are taken to be known. Thereafter small time steps are taken and the motion of the spheres during the step is calculated by integrating the acceleration of the particle in each direction. The particles accelerate due to external forces, such as gravity or contact forces when they interact with other particles or walls.

This interaction between particles is described by Newton's laws of motion. Figure 13 presents a schematic of the interaction between particles i and j. The contact forces are represented by a

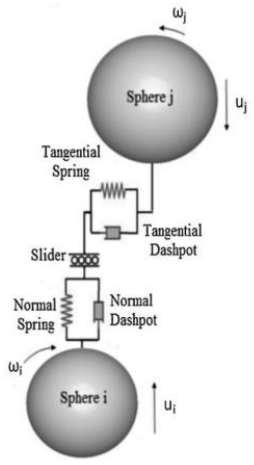

Figure 13: Contact model for interaction forces between particles

spring and the damping forces are represented by a dashpot, which correspond to the elastic and plastic nature of the particles. The tangential force is limited by the sliding friction, represented by the slider. The translational and rotational acceleration of particles are calculated by summing up all the forces and torques acting on the particles over a small time step. For a particle i which is in contact with K particles ($j = 1,2 \dots K$) the force equations may be derived as

$$m_i \frac{\mathrm{d}V_i}{\mathrm{d}t} = \sum_{j=1}^{K} \left(F_{\mathrm{cn},ij} + F_{\mathrm{dn},ij} + F_{\mathrm{ct},ij} + F_{\mathrm{dt},ij}\right) + m_i g \tag{4.1}$$

$$I_i \frac{\mathrm{d}\omega_i}{\mathrm{d}t} = \sum_{j=1}^{K} \left(T_{\mathrm{t},ij} + T_{\mathrm{r},ij}\right) \tag{4.2}$$

where V_i, I_i, ω_i and m_i are the translational velocity, moment of inertia, angular velocity and mass of particle i respectively.The translation of the particles is affected by normal and tangential components of the contact forces ($F_{\mathrm{cn},ij}$ and $F_{\mathrm{ct},ij}$), damping forces ($F_{\mathrm{dn},ij}$ and $F_{\mathrm{dt},ij}$) for particle pairs i and j and the gravitational force ($m_i g$). Likewise, the rotation is affected by torques due to the tangential force ($T_{\mathrm{t},ij}$) and rolling friction ($T_{\mathrm{r},ij}$). The values of the torques and forces are described by the contact model.

The Hertz-Mindlin approach is the most widely used contact model, where the normal contact force ($F_{\mathrm{cn},ij}$) is a function of the normal overlap ($\delta_{n,ij}$) between the particles. According to Hertz [32], the relationship is given by

$$F_{\mathrm{cn},ij} = -k_n \delta_{n,ij}^{3/2} \tag{4.3}$$

$$\delta_{n,ij} = R_i + R_j - \left(\vec{r}_i - \vec{r}_j\right) \cdot \hat{n} \tag{4.4}$$

$$\hat{n} = \frac{\left(\vec{r}_i - \vec{r}_j\right)}{\left|\vec{r}_i - \vec{r}_j\right|} \tag{4.5}$$

where $\vec{r}_i$ and $\vec{r}_j$ are the position of the particles and R_i and R_j are the radii, respectively, and $\hat{n}$ is the unit vector from i to j. The stiffness constant k_n is proportional to the equivalent Young's modulus (E^*) and square root of the equivalent radius (R^*)

$$k_{\mathrm{n}} = \frac{4}{3} E^* \sqrt{R^*} \tag{4.6}$$

$$\frac{1}{E^*} = \frac{\left(1 - \nu_i^2\right)}{E_i} + \frac{\left(1 - \nu_j^2\right)}{E_j} \tag{4.7}$$

$$\frac{1}{R^*} = \frac{1}{R_i} + \frac{1}{R_j} \tag{4.8}$$

E_i and E_j are Young's modulus and ν_i and ν_j are Poisson's ratio of the particles. The normal damping force ($F_{\mathrm{dn},ij}$) is proportional to the relative velocity of the particles (V_{ij}) along the normal direction ($\vec{V}_{n,ij}$)

$$F_{\mathrm{dn},ij} = -\eta_n \left|\vec{V}_{n,ij}\right| \tag{4.9}$$

$$\vec{V}_{ij} = \vec{V}_j - \vec{V}_i + \vec{\omega}_j \times R_j\hat{n} - \vec{\omega}_i \times R_i\hat{n} \tag{4.10}$$

$$\vec{V}_{n,ij} = \left(\vec{V}_{ij} \cdot \hat{n}\right)\hat{n} \tag{4.11}$$

where $\vec{V}_i$ and $\vec{V}_j$ are the translational velocity and $\vec{\omega}_i$ and $\vec{\omega}_j$ are the angular velocity of particle i and j. The coefficient η_n is given by

$$\eta_n = 2\sqrt{\frac{5}{6}}\beta\sqrt{S_n m^*} \tag{4.12}$$

β and S_n depend on the stiffness of the particles in normal direction,

$$\beta = \frac{\ln e}{\sqrt{\ln^2 e + \pi^2}} \tag{4.13}$$

$$S_n = 2E^*\sqrt{R^*\delta_{n,ij}} \tag{4.14}$$

$$\frac{1}{m^*} = \frac{1}{m_i} + \frac{1}{m_j} \tag{4.15}$$

where m^* is the equivalent mass and e is the coefficient of restitution. The tangential contact force ($F_{\mathrm{ct},ij}$) is proportional to the tangential overlap ($\delta_{t,ij}$)

$$F_{\mathrm{ct},ij} = -k_t\delta_{t,ij} \tag{4.16}$$

where k_t is the coefficient which depends on the equivalent shear modulus (G^*), equivalent radius and normal overlap ($\delta_{n,ij}$)

$$k_t = 8G^*\sqrt{R^*\delta_{n,ij}} \tag{4.17}$$

$$\frac{1}{G^*} = \frac{2-\nu_i}{G_i} + \frac{2-\nu_j}{G_j} \tag{4.18}$$

In Eq. (4.18), G_i and G_j are the equivalent shear stress for particles i and j. Cundall and Strack [33] proposed that the tangential overlap be given by summing up the relative tangential velocity ($\vec{V}_{t,ij}$) over the time (Δt) in which the particles are in contact with each other

$$\delta_{t,ij} = \int_0^{\Delta t} \left|\vec{V}_{t,ij}\right| dt' \tag{4.19}$$

$$\vec{V}_{t,ij} = \vec{V}_{ij} - \vec{V}_{n,ij} \tag{4.20}$$

The tangential damping force ($F_{\mathrm{dt},ij}$) is, in turn, given by

$$F_{\mathrm{dt},ij} = -\eta_t \left|\vec{V}_{t,ij}\right| \tag{4.21}$$

where the coefficient is defined as

$$\eta_t = 2\sqrt{\frac{5}{6}}\beta\sqrt{k_t m^*} \tag{4.22}$$

The tangential force is, however, limited by the Coulomb's friction law, so

$$F_{\mathrm{ct},ij} + F_{\mathrm{dt},ij} \leq \mu_s F_{\mathrm{cn},ij} \tag{4.23}$$

where μ_s is the coefficient of static friction. The tangential torque for particle i is

$$T_{\mathrm{t},ij} = R_i \times \left(F_{\mathrm{ct},ij} + F_{\mathrm{dt},ij}\right) \tag{4.24}$$

and the rolling torque is

$$T_{\mathrm{r},ij} = -\mu_r F_{\mathrm{cn},ij} R_i \omega_i \tag{4.25}$$

The time step for calculation is usually very small. If the time step is too big, the speed of energy transfer becomes large, resulting in unphysical deformation which may lead to energy 'generation'. The time step for the force calculation is therefore limited by the time taken for the energy to propagate through the particle by waves, known as Rayleigh waves. The limiting time step duration is called Rayleigh time [34].

$$T_R = \frac{\pi R\sqrt{\frac{2\rho(1+\nu)}{E}}}{0.163\nu + 0.8766} \tag{4.26}$$

It is usually recommended that the time step be 10-30% of the Rayleigh time. The time step is usually extremely small: in the simulations carried out in this thesis it was about 10^{-5} s. Therefore, simulating even short time sequences (say 5 s) requires a very large number of iterations (0.5 million). The main bottleneck for simulating different scenarios is, thus, the extremely large computation times. However, due to the nature of the method it can be parallelized very efficiently. Therefore, using a large number of computer processing cores can decrease the computation time considerably (Figure 14). If too many processing cores are applied, the decrease in processing time can be lost by overhead time, spent in communicating between processors. There are also other methods of decreasing simulation time. Decreasing the Young's modulus allows bigger time steps as the Rayleigh time becomes bigger which

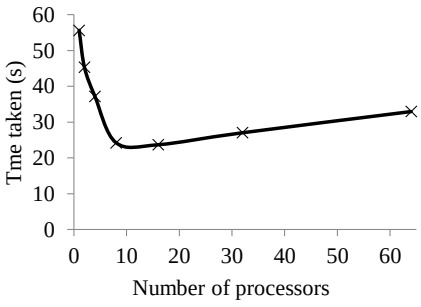

Figure 14: Computation time for a sample DEM problem as a function of number of processors

shortens the simulation time. Ueda et al. [35] found that Young's modulus has little influence on the layer structure in simulating the burden distribution and therefore the computation time may be reduced by artificially increasing the value of Young's modulus.

4.2 Properties of materials

The interaction between the particles depends on various material parameters. The following parameters are required for DEM simulation.

i. Density (ρ)
ii. Young's modulus (E)
iii. Poisson's ratio (ν)
iv. Coefficient of restitution (e)
v. Static friction (μ_s)
vi. Rolling friction (μ_r)

In this work, the density of the particles were experimentally determined. Other parameters like Young's modulus, Poisson's ratio, coefficient of restitution and friction coefficients between material pairs were taken from the literature [15, 36, 37]. Table 2 presents the values of each of the parameters used in the DEM simulations and their source. The coefficient of static friction between the coke particles was taken from literature and the coefficient of rolling friction was determined by conducting slump tests. For pellet particles, the inter-particle rolling friction coefficient was taken from literature, whereas the static friction coefficient was determined heuristically by comparing the layer profiles from DEM simulation with charging experiments, as values obtained from slump tests gave inconclusive results.

4.2.1 Slump test

The slump test setup consists of two halves of a metallic cylinder which were attached to hydraulic arms which retracted automatically at very high speed (Figure 15). The cylinder was filled with the material whose friction parameters were to be determined. When the arms retract, the material forms a heap, the contours of which give the angle of repose of the material (Figure 16, bottom). Next, a set of DEM simulations (Figure 16, top) were carried out with identical conditions, but with different values of the rolling and static friction. The angle of repose was also calculated for each combination of friction parameters.

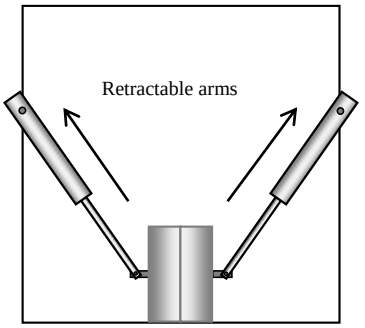

Figure 15: Schematic diagram of the slump setup

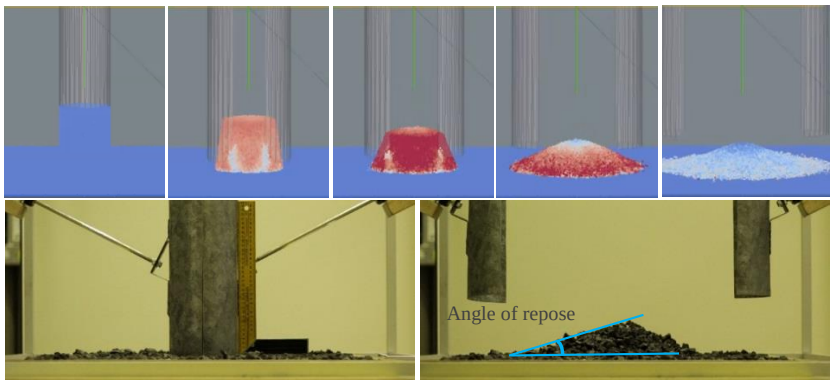

Figure 16: (Top) DEM simulation of the slump test at different time steps during release. The colors indicate the velocity of the particles, blue being lowest and red highest (Bottom) Slump test experimental apparatus in closed (left) and open (right) position, with the angle of repose of the heap indicated.

Figure 17 shows the angle of repose of the simulated condition as a function of the coefficient of rolling friction for different static friction coefficients. It may be seen that similar angle of repose values may be determined for different combinations of friction coefficients. Therefore, the value of the static friction coefficient was chosen from the literature and the corresponding rolling friction value was selected from these experimental findings.

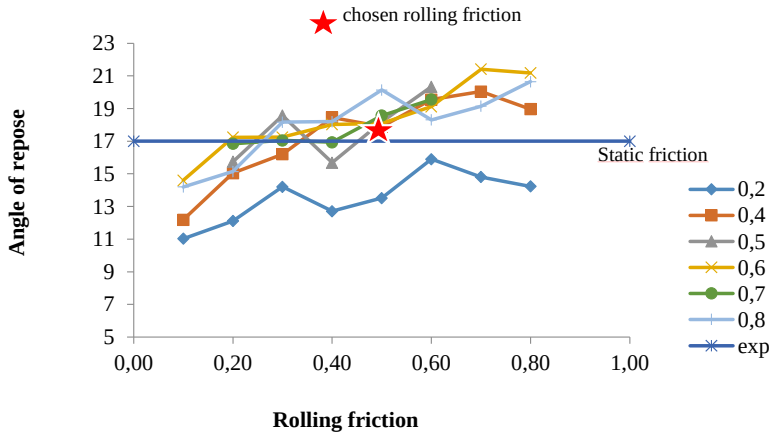

Figure 17: Effect of static friction and rolling friction on the angle of repose for coke particles

Table 2 Values of properties of the burden particles (experimental scale) used in the DEM equations. The asterisk (*) indicates measurement or experiment.

Material	Parameter		Value	Source
Pellet	Diameter		3 mm	*
	Density		4800 kg/m^3	*
	Poisson's ratio		0.25	[37]
	Young's modulus		25 MPa	[37]
	Coefficient of restitution	pellet	0.6	[37]
		coke	0.1	[36]
		steel	0.3	[36]
	Coefficient of static friction	pellet	0.7	*
		coke	0.43	[36]
		steel	0.5	[36]
	Coefficient of rolling friction	pellet	0.15	[37]
		coke	0.35	[36]
		steel	0.35	[36]
Coke	Maximum diameter	Large coke	12.5 mm	*
		Small coke	7.5 mm	*
		Center coke	18 mm	*
	Density		1050 kg/m^3	*
	Poisson's ratio		0.22	[37]
	Young's modulus		5.37 MPa	[37]
	Coefficient of restitution	coke	0.2	[15]
		steel	0.3	[36]
	Coefficient of static friction	coke	0.43	[37]
		steel	0.5	[36]
	Coefficient of rolling friction	coke	0.5	*
		steel	0.25	[36]

4.3 Particle shape consideration

Traditional DEM modeling is defined for perfect spherical particles. The motivation behind this assumption is that the interaction between spherical particles is one-dimensional, so it is computationally attractive. However, real particles are seldom spherical and their shapes may vary largely depending on the production technique of the particles. The literature proposes several approaches to solve the issue of particle shape [38]. Particles may be approximated using ellipses, polyhedrals or splines, but in all these cases the computational requirements for calculating the overlap between two particles grows considerably and for systems containing millions of particles this approach is not practical. Another approach is to simulate the system using Event Driven (ED) methods, which assume that the particles be absolutely rigid, which poses inaccuracy problems of its own. Another method is Discontinuous Deformation Analysis (DDA) which transforms a particle in contact using a 'stiffness matrix', similar to Finite Element Method (FEM), but this approach is not suitable for systems with a large number of particles.

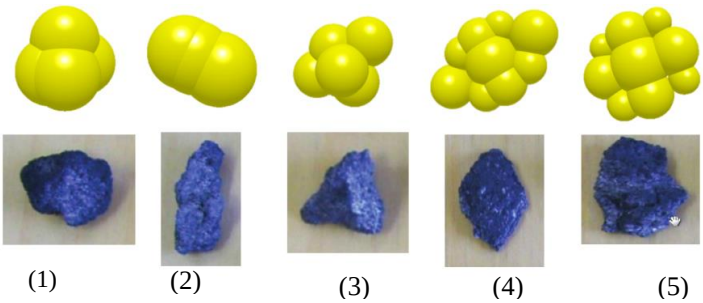

Figure 18: Coke particles of different shape and their representation using the clumped sphere model.

The most common method for accounting for particle shape is to construct the approximate shape of the particle using rigidly connected spheres, known as the clumped sphere or multi-sphere method. It has the advantage of being simple to implement and faster to calculate than any of the other alternatives. The multi-sphere technique still has its own disadvantages [39]. It is very difficult to implement flat surfaces reliably without using a very large number of spheres. Using many spheres, again, would increase the computational load as the positions of all the spheres need to be stored and considered in the contact model. It may also lead to interlocking of particles, which may show unphysical behavior. The ragged structure of the particles can also lead to inaccurate implementation of friction law. These aspects should be kept in mind when the clumped sphere method is used. Yet its simplicity and speed of implementation make it very attractive for DEM simulation of systems with non-spherical particles.

In the present work, two kinds of particles are used in DEM simulation, pellets and coke. Pellets are relatively smooth and round particles and can justifiably be regarded as spheres, but coke particles vary in shape and are far from spherical. Therefore, some sample coke particles were chosen as templates and the shapes were mimicked using the multi-sphere method (Figure 18). In all the simulations applying the multi-sphere method, a uniform size distribution was assumed and particles of each shape were created with equal probability.

The difference between the spherical and multi-sphere implementation of particles is here demonstrated by comparison of the results from simulation of a burden distribution charging program. The charging program consisted of three coke dumps, with small coke, large coke and the center coke (largest size), as well as pellets. The first layer of the charging program consisted of large coke which was charged at moderately high chute angles. Subsequently, two dumps of small coke were charged at two different positons, followed by two dumps of pellet at high chute angles. Figure 19 presents the isometric screenshots of the simulation results after charging the dumps. Subplots a-f (top row) present the results for the case where the coke particles were assumed to be clumped spheres, as discussed earlier, while subplots 1-6 (bottom row) show the results for the case where the coke particles were spherical. The results are seen to be qualitatively similar, but there are some differences: The largest difference is with the large coke particles which tend to roll to the center, if spherical particles are assumed, affecting all

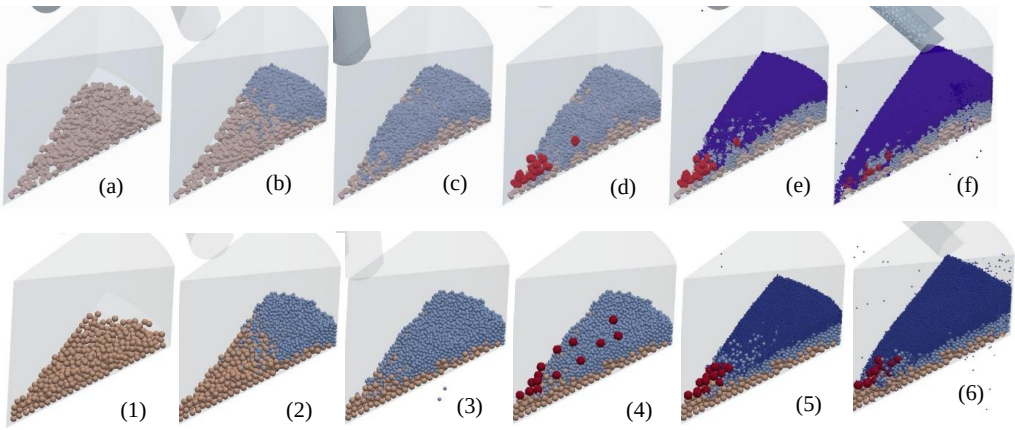

Figure 19: Isometric view of the DEM simulation using clumped sphere model (a-f) and spherical approximation (1-6) for coke particles, after charging each layer of a charging program.

the layers charged subsequently. The second small coke layer for clumped spheres (subfigure c) creates a distinct ring, while the spherical coke (subfigure 3) particles roll further making it difficult to distinguish the two layers. Furthermore, the final pellet layer covers the coke surface completely for spherical coke, while the clumped coke particles prevent the pellet layer from doing so. Top view comparison between the simulations is shown in Figure 20. When charging the first layer for spherical large coke particles the frictional torque is insufficient to create a heap, so most of the particles slide to the center of the simulated domain. This creates a vacancy near the wall which, in turn, is filled with pellet particles. Therefore, the simulation with spherical particles gives about 20% higher ore share at the wall. From this one may conclude that the spherical approximation of coke particles is not suited for this kind of studies, unless some other model parameter (e.g., friction coefficient) is adjusted to compensate for the undesired behavior.

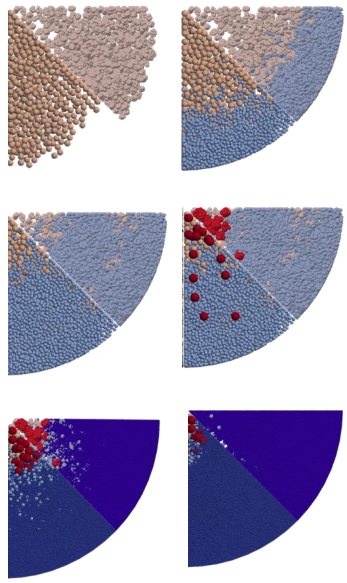

Figure 20: Top view comparisons DEM simulation using spherical model (lower sector) and clumped sphere model (upper sector) for coke particles, after charging each layer of the charging program.

5. Evolutionary algorithm

Evolutionary algorithms (EA) are a set of metaheuristic algorithms which have been inspired by the natural selection process in biology [40]. These algorithms are well suited for tackling optimization problems which are non-linear, discontinuous and non-differentiable. In ironmaking a large number of problems fall into this category and the EA has been successfully used for solving different kinds of problems [41].

Figure 21 shows the general scheme of an evolutionary algorithm. In this optimization technique, a population of candidate solutions for a particular objective function is generated randomly in the first stage, which is called the initialization. Each of the candidates represents a possible solution of the problem at hand and, thus, corresponds to a value of the objective function. Using the evolutionary algorithm new candidates are generated and tested whether they match the required conditions. For generating new candidates a set of candidates are chosen as 'parents' which participate in 'reproduction' resulting in 'offspring'. The reproduction stage is basically a combination of operators on the parent population, like recombination and mutation, which produces offspring. Individuals from this pool of offspring are selected using some criteria to continue the search for better candidates. The procedure is then repeated until a stopping criterion is satisfied. After a substantial number of iterations the population is expected to converge to a solution, which is taken to be the optimum.

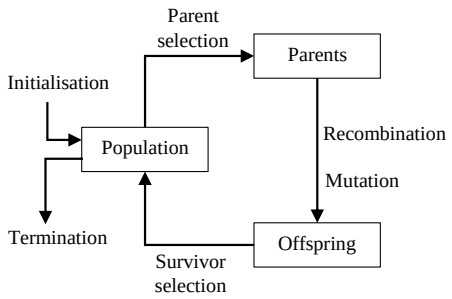

Figure 21: General scheme of Evolutionary Algorithms

In this thesis, an evolutionary algorithm was used for finding a combination of charging parameters to achieve a particular gas temperature profile at the top of the blast furnace. The current chapter therefore presents the basics of the particular kind of evolutionary algorithm, known as the Genetic Algorithm (GA) [42], which was used for this purpose.

5.1 Genetic Algorithm

Genetic algorithms are the most widely recognized type of evolutionary algorithms. They follow the general scheme of evolutionary algorithms: In a GA a candidate is represented as a string of numbers (usually binary, so referred to as bits) called a chromosome. The binary representation makes the optimization discrete in nature.

5.1.1 Recombination and mutation operators

The operators which are applied to the parent population in GA are inspired by the crossover and mutation mechanisms of biological chromosomes in nature. The recombination operator in GA is also called 'crossover' like its biological counterpart. In this method two candidates ('parents') are chosen from the population and sections of their chromosomes are swapped from a random position (Figure 22). The mutation operator (Figure 23), on the other hand, switches the value of a bit at a random position. Crossover produces offspring which are near the neighborhood of the parents so the search proceeds towards the nearest minimum. Mutation, on the other hand, produces offspring which may be away from the parent (Figure 24). The use of these operators creates candidates which represent new points in the search space. Mutation is different from crossover as it introduces greater diversity in the population so that minima further away from the parent population may also be identified. This gives the evolutionary algorithm higher probability of hitting the global optimum. The combination of these two operators makes this search algorithm suitable for tackling nonlinear and discontinuous problems, e.g. Mixed Integer Nonlinear Programming (MINLP) problems.

The difference between the crossover and mutation operators may be demonstrated using a simple example. A population of candidates is chosen, which represent points in a two-dimensional space. These points were converted into chromosomes of length 12. The chromosome was the binary representation of the coordinates combined end-to-end. Therefore, a point in this space, say (7, 19), was represented as

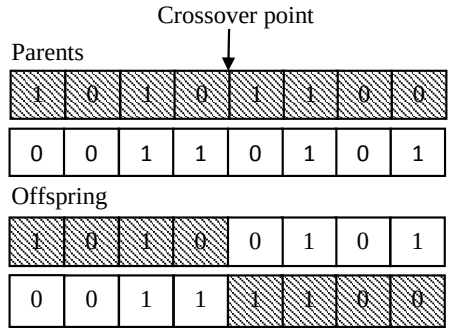

Figure 22: Crossover mechanism

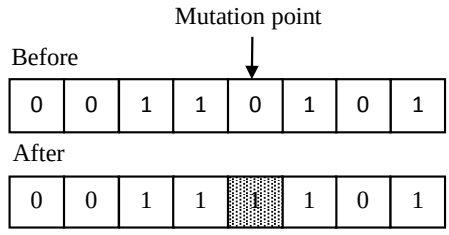

Figure 23: Mutation mechanism

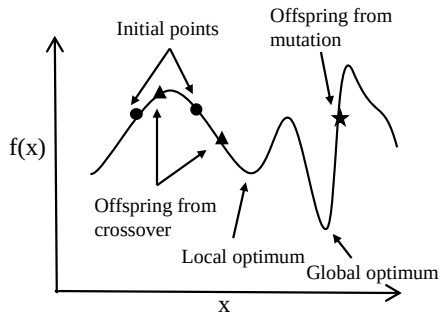

Figure 24: Local and global optimum for a minimization problem. Difference between mutation and crossover operators.

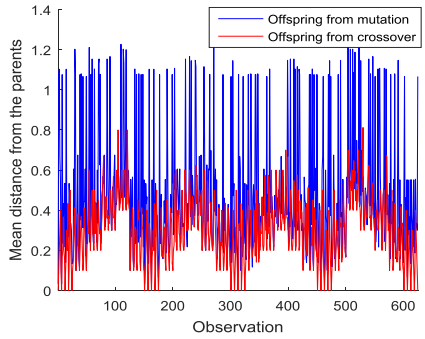

Figure 25: Distance of offspring from parents using pure crossover (red lines) and pure mutation (blue lines).

'00111-10011'. Thereafter, crossover and mutation operators were applied on the candidates at random locations to produce the offspring. The spatial distance of the offspring from the parents was calculated. Figure 25 shows the mean spatial distance of the offspring from mutation and crossover from their parents for each candidate. On average, the distances of the offspring from mutation are much higher than those from crossover, which demonstrates the difference in the nature of the two operators.

There are different crossover mechanisms, such as *n*-point crossover, uniform crossover, real valued crossover (for chromosomes with real values) and mutation mechanisms such as bit-flipping, non-uniform mutation, etc. The operators should be chosen based on the nature and complexity of the problem.

5.1.2 Selection

After creating offspring population, candidates for the next iteration are selected. The chromosomes are evaluated using the objective function. The function values are then scaled and ranked according to their fitness (goodness) of the solution. In evolutionary methods, it is not necessary that only the best candidates are chosen for the next iteration. The surviving population may consist of both good and not so good candidates to preserve diversity; otherwise the search may lead to premature convergence to a local minimum and the global optimum will not be found. A healthy diversity in the population is achieved by probabilistic selection techniques such as tournament selection and roulette wheel selection. In tournament selection, a set of members are chosen from the population and the best is selected and added to the new population. This is repeated until the target population size is achieved. In roulette wheel selection, the probability of selecting an offspring depends directly on the fitness of the candidates. In elitist selection, the best candidates from the parent population are always preserved and replace the worst candidates from the offspring population.

The above operations (crossover, mutation and selection) are repeated until a target fitness is achieved or a predefined maximum number of iterations, called generations, have been reached. At the end of the iterations, the population should converge to the best solution in the domain (Figure 26). The population from the final iteration should contain the optimum, and possibly other promising candidates, as well.

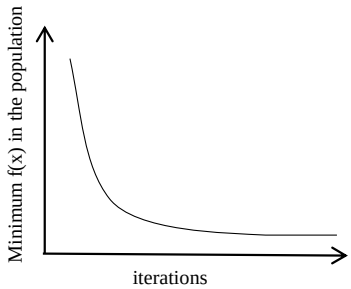

Figure 26: Convergence of the algorithm for a minimization problem with objective function f(x).

6. Burden distribution modeling

With increasing energy costs, depreciating quality of raw materials and lowering of coke rates in the ironmaking process, a greater understanding of the burden distribution becomes essential for accurate control of the blast furnace. The main issue in controlling the burden distribution is to obtain proper radial distribution of ore and coke in the furnace and ensure control over the size segregation, since these affect the gas permeability and thus the gas flow distribution. The charge can be fed into the furnace via different distribution mechanisms (Sec. 3.1), the most common of which is the bell-less top charging system. After being charged, the burden slowly descends into the furnace where the ore is reduced by the ascending reducing gas. The burden preserves its physical properties until it reaches the cohesive zone where the ore starts to soften and melt.

In this chapter, different models developed in literature are discussed, focusing on each stage of burden handling.

6.1 Modelling of top bunker and hopper system

Hopper systems (Figure 27) are used in almost all industries where granular material is stored or transported. After the raw materials are weighed in a surge hopper, the charged amounts are fed into skips or on a conveyor belt, and are transported to the top bunker of the furnace. The storage bins, surge hoppers and the top bunker are usually funnel type hoppers. The flow behavior in funnel type hoppers has been studied extensively.

The flow rate from the hopper is primarily a function of discharge orifice, the taper angle of the conical base and possible inserts in the hopper for a particular type of particle and hopper material [43]. These parameters decide the flow pattern inside the hopper [44]. It may either have a funnel type flow or plug flow. In plug flow (also called mass flow) the particles uniformly descend across the whole bunker, whereas in funnel flow a dead zone is created near the walls (Figure 28). Continuum methods have been traditionally used to predict the nature of the flow. The most well-known is Jenike's model which predicts the boundary between plug flow and funnel flow based on the internal friction angle, wall friction angle and taper angle of the hopper [45].

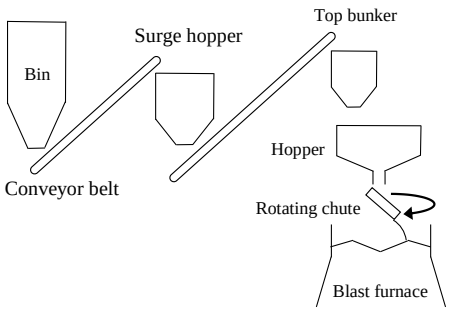

Figure 27: Schematic of hopper system

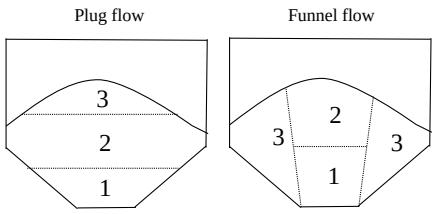

Figure 28: Discharge order for plug flow and funnel flow.

Predominately funnel flow has been observed in blast furnace hopper systems [21, 46].

Real life particles are seldom monodisperse and also often vary in shape. Size segregation at any stage of the hopper system is relegated to the next before the material is charged into the furnace. In such cases, funnel flow regime causes size segregation, which leads to discharge of non-uniform particle distribution over time (Figure 29, [47]). When using a rotating chute for burden distribution, the charging is not truly axisymmetric and the particle size may also vary according to where the charging process has started. It is, therefore, important to control the segregation in the flow.

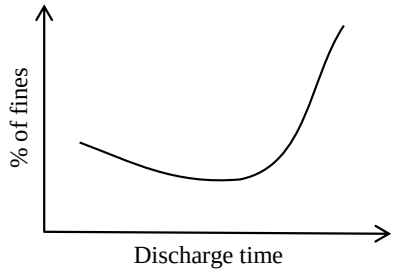

Figure 29: Particle segregation during discharge from hopper

Recently, DEM methods have been used extensively to model hopper charging and discharging for various applications. Different aspects of the discharging process have been studied extensively, such as prediction of wall stresses [48], effect of particle shape [49] and discharge dynamics [50]. The authors have suggested different ways of reducing segregation: Yu and Saxén [47] concluded that segregation may be reduced by reducing the wall-particle friction or the amount of fines. Jung and Chung [46] redesigned part of the hopper system and utilized the segregation behavior to control radial size distribution in the blast furnace and to improve the gas flow conditions.

Usually small quantities (< 5 % wt.) of small coke (also called 'nut coke') is mixed with ore to improve permeability of the ore layer, but the amount is limited as in higher amounts segregation may make burden distribution control difficult. A more accurate control of the size segregation in the hopper system facilitates the charging of a higher coke fraction in the ore layer, known as mixed coke charging. This has been demonstrated to improve the reducibility of ore and has led to reduction of RAR by 3 kg/t hot metal in some trial runs with actual furnaces [51]. In order to minimize segregation during material handling, the coke is mixed on the conveyor belt right before charging into the furnace rather than in the surge hopper [21]. Also, modifying the hopper design may yield proper mixing [52].

6.2 Modelling of particle trajectory

Bell-less top with a rotating chute (Sec. 3.1.2) is the most common modern burden distribution system used. The particles are emptied from a hopper system into a rotating chute which, in turn, distributes the material at a particular radial position into the furnace.

The particle trajectory decides the impact point on the burden surface, which is useful for burden distribution calculations. The path of the particles may be divided into three distinct zones (Figure 30).

i. Material falling from hopper onto the chute.

ii. Material sliding along the chute.

iii. Free fall from the chute tip.

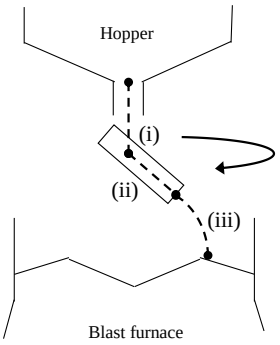

Figure 30: Particle trajectory zones

Some authors have assumed that the particles are stationary when they leave the hopper [53, 54]. Radhakrishnan and Ram [43], on the other hand, used the following approximation for calculating the velocity at the end of the hopper

$$v_{hopper} = \frac{(D-d)^{2.5}}{4D^2}\sqrt{g\left(\frac{1-\cos\beta}{2\sin^3\beta}\right)} \qquad (6.1)$$

where D is the orifice diameter, d is the particle diameter, g is the acceleration due to gravity and β is the acute angle between horizontal and the cone wall. The particles fall on the chute under gravity through the 'downcomer' and hit the chute. The velocity on reaching the chute is calculated by solving the energy conservation equation. Investigators sometimes apply a correction factor due to the internal collisions in the particle stream [43, 55]. In simplified mathematical models the collision of particles with the chute is assumed to be perfectly elastic, so the particles lose their velocity perpendicular to the chute.

As the particles slide down the chute due to gravity, friction and Coriolis forces act on the particles. The chute surface is not smooth and may be ribbed to reduce chute wear, inducing a braking force on the particles. Therefore, the 'effective' chute length is sometimes considered to be more than the actual chute length to account for the braking force [43]. Some authors have also calculated the deflection of the particle stream in the chute due to the Coriolis force [53, 56]. The velocity distribution along the chute cross-section becomes more uniform as the particles slide down the chute [37, 57]. Particle shape affects the angular velocities, so it influences the overall velocity of the stream [37].

If the particle stream consists of a broader size distribution, the larger particles tend to 'float' on the smaller particles as they are discharged from the chute [58]. Therefore, the bigger particles land near the wall whereas the smaller particles enter closer to the furnace center (Figure 31) [59]. Sometimes a damper is added at the end of the chute to reduce particle segregation [58]. Also the width of the burden flow increases due to the Coriolis force [56, 60]. The heavier particles also land slightly nearer to the wall due to higher velocity at the end of the chute tip.

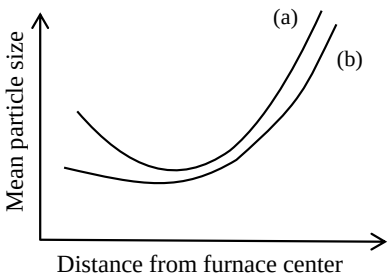

Figure 31: Radial particle segregation after discharge on a flat surface depending on the charging position: Near the furnace wall (a) or center (b).

After leaving the chute tip, the particles flow under gravity until they hit the stock line/burden surface. The particles move through the ascending gas which may provide some buoyancy and drag force, causing the fines to divert from the furnace center [56, 61]. However, the effect of the gas flow is often ignored. Most authors calculate the trajectory as a parabola whose coefficients are calculated using Newton's law [53, 54, 62]. The material stream may also be assumed to have some width described with an upper and lower trajectory [43, 55]. Figure 32 shows the radial distribution of mass as the material falls out of a chute and approaches the burden surface.

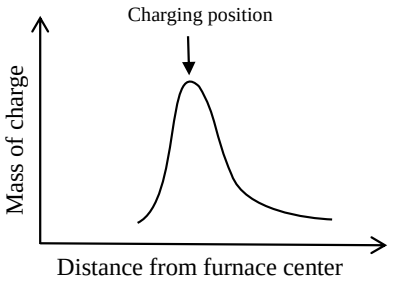

Figure 32: Distribution of charge as the material stream approaches burden surface.

6.3 Modelling of burden formation

As the particles fall from the chute on the burden surface they redistribute into a heap. Most mathematical models are two-dimensional assuming axial symmetry. Therefore, the upper surface or cross-section of the arising heap is usually modelled either by combination of two [43, 54, 55] or more [63] straight lines or more complicated curves given by cubic equations [64] or normal distributions [27, 65] (Figure 33). More complicated representation methods result in more realistic (looking) burden surfaces, but the computational effort grows and problematic numerical conditions may have to be imposed.

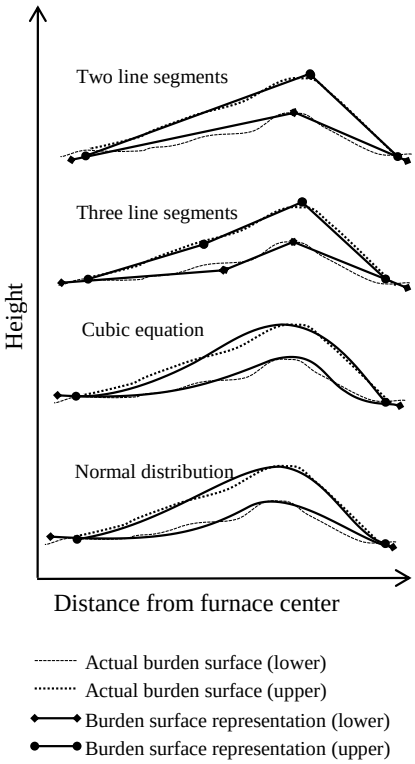

Figure 33: Burden shape approximation

For the straight-line representation the slope of the lines depends mainly on the material properties and position of charging. Park et al. [55] used

$$\alpha = CA_{max}\frac{d^{0.05}}{4f^{0.05}} \tag{6.2}$$

$$\beta = \alpha\left(\frac{\frac{D}{2} - X^{1.4}}{5.8}\right) \tag{6.3}$$

for calculating the inner repose angle (α) and the outer repose angle (β) for their scaled model experiments. These are the acute angles formed by the line segments with the horizontal. A_{max} is the

maximum angle of repose for the material, d is the particle diameter, D is the throat diameter, X is the intersection point of the trajectory and the burden surface and C is a constant. f is the shape factor, which is the ratio of minimum and maximum diameters across the particle. Therefore, the inner repose angle is proportional to the particle size and roughness of the particle. The outer repose angle decreases as the falling point approaches the wall. This has been observed experimentally and may be explained by the fact that the mass is spread towards the wall (Figure 32). The apex of the layer made of line segments is usually located on the trajectory. Fu et al. [66] have used a different formulation for the outer repose angle (β) which is correlated to the product of chute inclination angle (θ) and rolling coefficient (k),

$$\beta = \alpha - k\theta \tag{6.4}$$

The burden surface may also be represented by a cubic equation. The surface (y) is represented by a function of radius (r)

$$y(r) = a_1 r^3 + a_2 r^3 + a_3 r + a_4 \tag{6.5}$$

where the coefficients a_1-a_4 are determined empirically. In a similar way, the normal distribution may also be used for representing the surface

$$y(r) = Ae^{-\left(\frac{r-B}{C}\right)^2} + Dr + E \tag{6.6}$$

where A is proportional to peak height, B is peak location, C gives the spread of the heap, D compensates for the influence of the base profile and E is related to the stock level.

After the shape of the burden surface is defined, the location of the surface is found by equating the volumes of the heap and the dump. This step, which involves locating the intersection of the new burden surface with the old one, induces higher computational load for more complicated representations. Shi et al. [67] utilized different schemes for modeling the burden surface and evaluated them by comparing the results with experimental burden surfaces determined by image processing [68]. They found different schemes to be accurate for different charging sequences, but concluded that the models were more accurate when repose angles were considered to be a function of charging positon.

In most models axial symmetry is assumed, but chute rotation direction can also be an important factor in causing cross-sectional inhomogeneity under charging. Xu et al. [69] advocated alternating the hoppers without altering the charging direction for achieving the most uniform burden surface.

Most of the mathematical models do not consider effects of charging different kinds of material on top of each other, like mixed layer formation, percolation and coke collapse.

6.3.1 Mixed layer

In reality, the layers are not distinct as presented in Figure 33, but there is a region between the layers which contains particles of both types. This region is larger when the particle sizes are very different and small particles are charged on large ones. This is because the smaller particles penetrate more into the void between larger particles. This phenomenon was measured experimentally by Kajiwara et al. [70] using magnetic impedance techniques. The voidage in the mixed region may be much lower than that of the individual layers [71]. With reduced coke consumption, the coke layers in the blast furnace are becoming thinner and the effect of mixed layers is becoming more predominant.

6.3.2 Coke collapse

Coke particles are much lighter than ore, so whenever ore is charged over coke, especially at higher chute angles, the coke burden surface may deform or collapse depending on the kinetic energy carried by the stream of ore particles. This results in a burden distribution which can be much different from the expected one.

In one of the earliest studies on this phenomenon, Kajiwara et al. [70] arrived at an expression for the increase of coke layer height (ΔL_c , expressed in meters) at the center of the furnace with a bell-top charging

$$\Delta L_c = 3.49 \times 10^{-4} E_M - 136 \tag{6.7}$$

E_M is the formation energy, expressed in kg m^2/s^2, which was taken to be the total energy (kinetic and potential) energy of the particle stream hitting the coke surface. The authors also concluded that the affected region where the height of coke layer increased corresponded to a radius 0.36 times that of the furnace throat.

Some authors [72, 73] have studied the effect of charging heavy particles on lighter particles through an orifice experimentally and by DEM, concluding that the crater size depends on the ratio of input energy (E_{input}) and inertial energy (E_{inertial}).

$$S_{\text{crater}} = 3.54\, e^{\frac{-20.83\, E_{\text{inertial}}}{E_{\text{input}}}} \tag{6.8}$$

$$E_{\text{input}} = \frac{1}{2} m_t v_0^2 + m_t g H \tag{6.9}$$

$$E_{\text{inertial}} = m_b g d_b \tag{6.10}$$

S_{crater} is the dimensionless crater size, m_t and m_b are mass of particles in the top and base layers, v_0 is the velocity (at the end of chute), H is discharge height and d_b is the diameter of particles in the base layer. The crater size is defined as

$$S_{\text{crater}} = \frac{A}{A_0} \frac{d_b^2}{d_t^2} \tag{6.11}$$

where A is the crater area, A_0 is area of the orifice and d_t is the diameter of particles in the top layer.

The deformation of the coke layer due to the ore stream also depends on the energy carried by the particle stream and the shape of the underlying coke layer. If the underlying coke layer is stable enough, a collapse might not happen and only a part of the layer is displaced by the ore particles. The two forms of failure are termed 'impact failure' and 'gravity failure' respectively (Figure 34). The stability of the underlying coke layer is quantified using a coke collapse model [74-76], as discussed in Section 7.7.

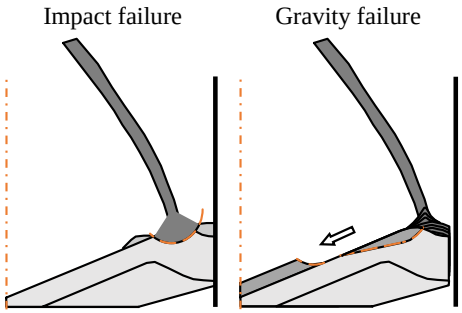

Figure 34 : Impact failure and gravity failure

6.4 Modelling of burden descent

The reduction of iron ore in the blast furnace is a continuous process. The solid burden is consumed continuously at the lower part of the furnace along with melting (of ore) and combustion and dissolution (of coke). The iron bearing burden reduces to iron and starts melting at the lower end of the cohesive zone, and the coke is mainly consumed in the raceways. Pathlines for the solids are schematically illustrated in Figure 35.

The burden descent is not much affected by the gas flow and therefore the solid streamlines may be assumed independent of the gas flow conditions. The descent velocity is usually assumed to be a function of ore-to-coke distribution, shape of the deadman and furnace irregularities, such as scaffolding.

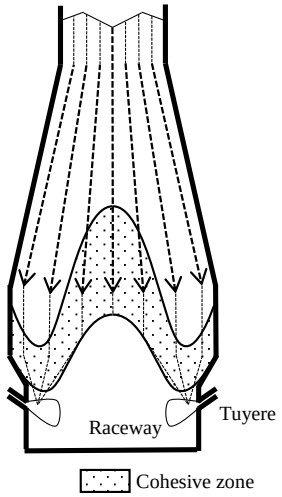

Figure 35 : Solid pathlines (schematic representation)

In the literature, the burden descent has been modeled using the geometric profile model [77], the potential flow model [66] or by descending the layers one at a time [54]. Geometric profile models assume uniform velocity along all the radial points. In reality the radial velocity component may vary along the radius of the furnace due to the presence of the deadman and non-uniform reduction along the radial direction. Potential flow models tackle this problem by solving equations for the potential function (ϕ_s) along the height (y) and radius (r),

$$\nabla \cdot (\rho_s K_b \nabla \phi_s) = S_s \tag{6.12}$$

$$v_{s,y} = -K_b \frac{\partial \phi_s}{\partial y} \tag{6.13}$$

$$v_{s,r} = -K_b \frac{\partial \phi_s}{\partial r} \tag{6.14}$$

where ρ_s is the burden density, S_s is the burden consumption rate, $v_{s,y}$ and $v_{s,r}$ are solid velocities along height and radius, respectively. K_b is the relative descending speed of the burden which depends on the relative radius of the point, $\frac{r}{r_{max}}$. Instead of solving this higher order equation, another approach can be made where the layers are descended in sequence considering the radial velocity distribution.

The descending velocity is influenced by the ore-to-coke distribution, where, higher ore content increases the burden velocity in that region [78]. It is difficult to gain better knowledge about the descent behavior in actual furnaces because of the lack of measurements in the lower part of the furnace other than stockrod and radar measurements. Therefore, a large number of DEM studies [35, 79, 80] of the whole blast furnace have been performed for understanding the descent behavior under different conditions and for describing the corresponding stresses on the blast furnace walls. Fan et al. [81] studied the effect of furnace size on the burden descent and found some differences in descent velocities close to the deadman for the furnaces above 5000 m^3 because of larger relative deadman size.

Segregation behavior is also expected during burden descent mainly due to the change in diameter of the furnace. Some authors [82, 83] used a scaled setup with movable base and wall to evaluate the effects of changing diameter, physical properties and coke shape as the burden descends into the furnace. They found higher percolation of smaller iron ore pellets near the wall.

6.5 Gas flow modeling

Blast furnace aerodynamics has been studied widely by different authors [12, 84-86]. They have considered all or combinations of the factors which are of interest, including thermal conditions, solid flow, gas flow, liquid flow and chemical reactions. The solid flow has often been modeled separately independent of the gas flow and is relatively straight forward (Sec. 6.4) except in the cohesive zone [87]. Gas flow in the upper lumpy part of the furnace is a function of the pressure drop, heat exchange between solid and gas and the porosity of the bed. It is easier to model the flow in the upper part than in the lower parts where melting occurs along with a large number of physiochemical reactions. The latter region begins with the cohesive zone and modeling of this region is complicated [87]. Numerous fundamental assumptions have been made by different investigators to make the calculations easier. In the raceway region the coke is converted to mainly carbon monoxide and the conditions in this region have been a topic of study in itself [88-90].

The flow simulations in the furnace are carried out by numerical methods, where the furnace is divided into small homogeneous computational grids. The solution of an individual grid point is affected by the conditions in the neighboring computational points, except the points at the boundary of the computational grid, where the boundary conditions are applied. Proper boundary conditions are very

important for the reliability of the numerical results and different authors have applied different assumptions. It should be stressed that it is extremely difficult to verify the results due to lack of access to the interior of the furnace.

Blast furnaces are commonly simulated as a packed bed, through which the reducing gas flows upwards. The pressure drop gradient across the computational unit of a packed bed is calculated using the Ergun equation [91] which is represented in vector form as

$$-\nabla P = \overrightarrow{v_s}\left(\frac{150\mu(1-\varepsilon)^2}{\varepsilon^3 D_p^2} + \frac{1.75\rho(1-\varepsilon)}{\varepsilon^3 D_p}|\overrightarrow{v_s}|\right) \tag{6.15}$$

where μ is the dynamic viscosity of the gas and ρ the density of the gas. D_p is the diameter of a spherical particle of volume equal to the particle, known as equivalent spherical diameter. $\overrightarrow{v_s}$ is the superficial velocity, which is the velocity of the gas assuming the same volume flow rate through an empty furnace volume and ε is the bed void fraction which depends on the burden composition. This equation may be used to evaluate the pressure drop in each direction of the computational domain.

The pressure drop equation is solved together with the continuity equation given by

$$\nabla \cdot (\rho\overrightarrow{v_s}) = 0 \tag{6.16}$$

The two equations are solved using iterative techniques to minimize the residuals.

The gas temperature in the furnace depends on heat transfer and chemical reactions. Variables such as viscosity, density etc. depend on temperature and composition of the gas, so each of these variables need to be estimated accordingly.

The burden has a layered structure and the interface of two layers with different particles forms a mixed layer which has a much lower voidage than the layers. Therefore, as the number of layers and layer interface increases, the resistance to the gas flow increases. The resistance is proportional to the ratio of the particle sizes making up the interface [92] as increasing the particle size ratio increases the particle-particle contact and results in better packing at the interface. Higher gas flow rates, in turn, may lead to lowering of the voidage because the smaller particles have lower penetration [93].

The conditions in the lower part of the furnace do not radically affect the gas flow in the upper part of the furnace: The gas follows the path of least resistance, so any major pressure drop along the radial direction leads to 'redistribution' of the gas [94]. The redistribution effect also results in a zig-zag path of the gas flow

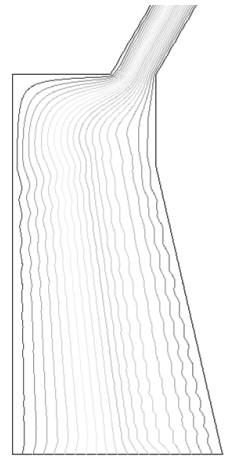

Figure 36: Zig-zag path followed by gas

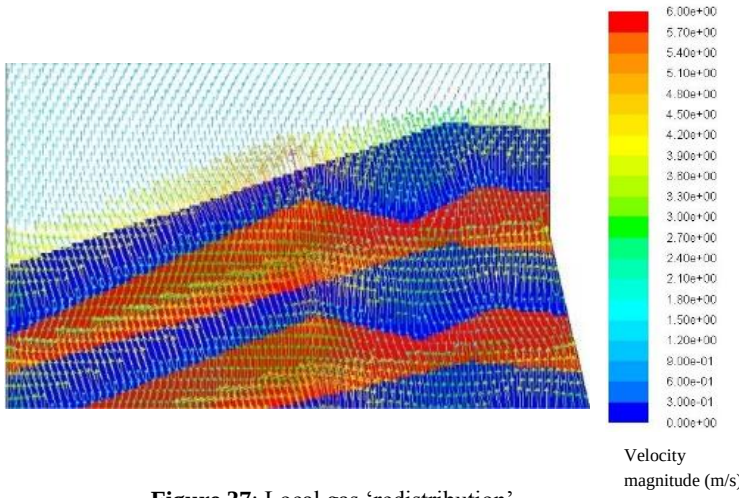

Figure 37: Local gas 'redistribution'.

(Figure 36). In the less porous ore layer, the gas encounters lower resistance by turning perpendicular to the layer surface, thereby shortening the travel distance in the layer. The layer structure therefore affects the local gas flow direction and flow rates [95]. Figure 37 shows velocity vectors at different positions close to the burden surface. This overall redistribution of gas in the lumpy zone was used as a motivation for describing the gas flow in the upper furnace part without simulating the lower part of the furnace in the present work [96], simultaneously neglecting the effect of chemical reactions on the conditions.

Recently, several authors [97-99] have utilized Computational Fluid Dynamics for three-dimensional modelling of the blast furnace. In these models, the burden descent in the whole furnace has to be modeled, including the coke motion below the cohesive zone and the coke consumption in the raceways. The results of such models provide a very detailed description of the in-furnace phenomena and of the individual phases (solid, liquid and gas) which may be characterized in terms of temperature, velocity, volume fraction and component distributions. Such findings may be used to further improve the control of the whole blast furnace operation by gaining a deeper understanding of the interrelation among the different phenomena. However, the lack of verifying measurements and the non-ideality of the true process still pose serious issues for the practical control of the blast furnace.

7. Models developed

In this thesis, the author has made an attempt to shed light on certain aspects of the burden distribution in a blast furnace with a bell-less charging system using mathematical modeling, supported by small scale experiments. Figure 38 presents a schematic diagram describing the different parts of the work collected in the thesis. The numbered papers refer to the publications in the Appendix.

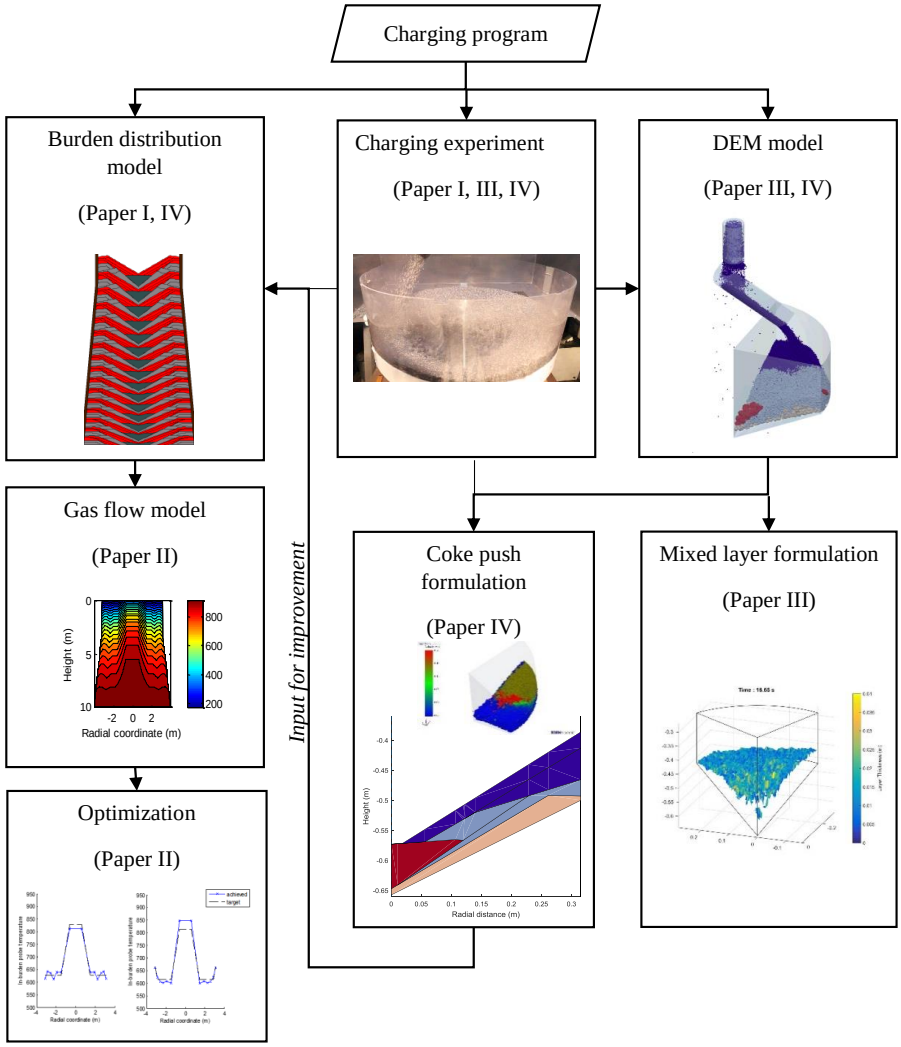

Figure 38: Flowchart depicting the models developed and approaches made in this thesis

In the first stages of the work, a simplified mathematical model for burden distribution estimation in a bell-less top blast furnace was created based on a similar earlier work on bell-top charging [63]. Although the basic principles were similar, the work included a number of new aspects and

improvements, especially pertaining to the burden descent model. New strategies were especially required to handle the complexity introduced due to thin layers. The first article, Paper I, on the list of publications (cf. page vi) details the burden distribution and descent model, and compares the simulation results with the experiments performed using a small scale charging model. This mathematical model is a simplified 2D model based on a large number of assumptions, yet the results were found to correlate reasonably well with the experimental results. The lack of accuracy was compensated for by the speed of calculation. It takes about 20 s to run a burden distribution and descent simulation of a charging program with 20 layers using a processor with a speed of 3.30 GHz. The speed of calculation allows the user to run multiple simulations of the burden distribution before deciding the one best suited for a particular operation. Therefore, the industrial partner of the work (SSAB Europe, Raahe) has utilized the model through a GUI implementation and has found the tool useful for the design of charging programs.

The burden distribution model enabled the calculation of the burden material distribution in the furnace, which makes it possible to estimate the gas permeability distribution. A simplified gas flow model was therefore developed in Paper II to calculate the gas distribution. This model was partly based on the ideas presented in [100]. However, the earlier model was extended to predict the gas temperature on the top of the furnace assuming an isobaric inlet conditions for a simulated burden distribution. As described in section 3.3, the design of burden distribution programs is a complicated task with numerous alternatives. Paper II presents the results of a work where the burden distribution model was used for designing charging programs with the goal to achieve a particular gas temperature profile. This design task was tackled using a genetic algorithm.

Even though the simplified mathematical model gives insight about the burden distribution, it cannot accurately describe complex interaction of the charged materials, which would be required for a detailed understanding of the burden distribution process. Therefore, a DEM model was developed and utilized to analyze the charging process more closely. Model charging programs were simulated using DEM and small scale charging experiments in the laboratory were used to verify the simulation results. In the third publication (Paper III), the phenomenon of mixed layer formation on charging particles of different characteristics on each other was analyzed. The mixed layer was defined and quantified in this work. In the final article (Paper IV), the conditions at the burden surface during charging were analyzed more deeply, by simulating several model charging programs and focusing on the interaction between the heavier pellets charged on the lighter coke. Conditions for collapse of the coke layer were identified and slope stability theory was used to quantify the risk of coke collapse for different charging programs. In the above studies, size segregation has not been considered.

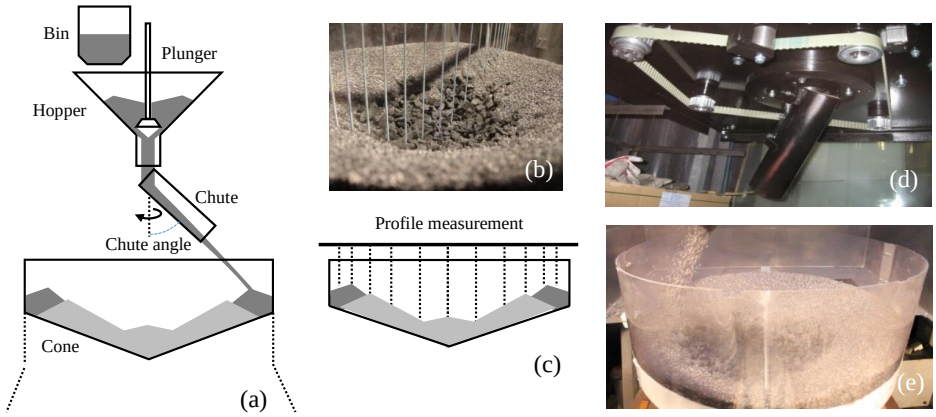

Figure 39: (a) Schematic diagram of the burden charging setup. (b) Profile measurement device. (c) Schematic profile measurement strategy. (d) Small-scale model of bell-less charging. (e) Scaled model of the charging throat.

7.1 Charging experiment (Paper I, III, IV)

Charging experiments in the work were carried out using a physical model (Figure 39) of the bell-less top burden charging apparatus with a rotating chute built before this work was started [101]. The charging device consists of a bin which holds the dump until it is emptied into the hopper, where a plunger valve controls the flow rate of particles, which fall on the rotating chute, eventually forming a ring of particles on the burden surface. As the density, size and characteristics of the particles are different, therefore the clearance of the plunger was adjusted to create a complete ring of each dump of particles charged. The angle of the chute can be adjusted prior to charging. The charging angles were discretized similar to the industrial charging setup (Table 3). The particles falling from the chute are charged onto a steel cone which is mounted into a cylindrical throat section made of transparent polycarbonate. A layer of coke particles was glued on the cone to create an initial burden layer mimicking a coke layer with an inclination similar to the angle of repose of coke. This setup was applied to create identical initial conditions for the experiments and to avoid the arduous filling procedure.

The physical model was scaled 1:10 of the dimensions of an actual Finnish furnace. Applying the same scaling factors to the particles would have induced unwanted effects, such as strong dust formation and unrealistic intra-particle forces, so a scale of 1:4 was instead chosen for the particles. Due to this approximation, some of the observed phenomena were exaggerated or underreported compared to the actual conditions. This issue was recognized before drawing definite conclusions from the results. The pellet particles were provided by LKAB, Sweden, while Ruukki Oy (present SSAB Raahe) provided the coke particles for the experiments. The raw materials included three sizes of coke, large coke (10 mm - 16 mm), small coke (5 mm - 10 mm) and center-coke (16 mm - 20 mm), and iron ore pellets (3 mm). The throat diameter of the model is 0.63 m and the distance between the chute tip at its lowest position and the stockline was set to 0.2 m. The burden profile measurement was carried out by a

mechanical device (Figure 39, b and c), by which the burden layer height at different radial points was measured after charging each layer. The measurements were taken along two of the throat diameters, away from the starting position of the coke dump, as it may induce errors. After measuring, the 'furnace' was lowered hydraulically until the aim charging height was reached. This procedure was repeated for each charged ring of the program.

Table 3 Chute positions and corresponding chute angles

Chute position	1	2	3	4	5	6	7	8	9	10	11
Chute angle (˚)	15.0	26.7	29.9	32.7	35.1	37.5	39.6	41.7	43.7	45.6	47.4

7.2 Burden distribution and descent model (Paper I)

The burden distribution and descent model developed was based on simple mechanics and was aimed at producing a fast prediction of the burden structure inside a blast furnace. The burden distribution model predicts the flow of particles from the hopper to the formation of the layer. The descent model describes the structure of the layers as they descend into the furnace shaft. The basic equations used for the two models are discussed below.

7.2.1 Burden distribution model

Figure 40 presents a schematic diagram of the burden distribution domain. The flow of the material from hopper to the layer surface was modelled for a single particle and the parameters were tuned, so the radial position where the stream hits the burden surface at different chute angles agreed with values observed in small-scale experiments. In this model the dump is assumed to be stationary as it leaves the hopper. Some other authors who took similar approaches [43] have used a different formulation (eq. 6.1) for the velocity at the exit from the hopper. However, they eventually include a factor to reduce the velocity artificially, because most of the kinetic energy of the particle is lost as it collides with the chute. The current approach saves computation time as the velocity of the particle on hitting the chute is not of interest for the goals of the model. The velocity of the particles as it reaches the chute (v_0) is therefore expressed as

$$v_0 = \sqrt{2g\left(h_0 + \frac{d}{\sin\alpha}\right)} \tag{7.1}$$

where g is the acceleration due to gravity and d, h_0 and α are defined in the left part of Figure 40. After striking the chute, the particles are assumed to lose their velocity perpendicular to the chute. The force balance of the particle (cf. insert in the left part of Figure 40) moving down the chute at a distance x along l gives the acceleration of particles (a) along the chute

$$a = g\sin\alpha + \omega^2 x\sin\alpha\cos\alpha - \mu(g\cos\alpha - \omega^2 x\sin^2\alpha) \qquad (7.2)$$

where ω is the rotation speed of the chute and μ is the friction coefficient between the particle and the chute. The friction coefficient was exaggerated to consider particle collisions. The velocity at the end of the chute (u_0) was found by integrating the acceleration along the distance, l, travelled by the particle along the chute.

$${u_0}^2 = {v_0}^2\cos^2\alpha + \omega^2 l^2\sin\alpha\,(\sin\alpha + \mu\cos\alpha) + 2gl(\cos\alpha - \mu\sin\alpha) \qquad (7.3)$$

It is assumed that there is no rolling and that the only sliding friction that occurs is between the particles and the chute. The velocity is used to calculate the falling trajectory of the particles with reference to the axes (cf. Figure 40) and is given by

$$z = -r^2\left(\frac{g}{2{u_0}^2\sin^2\alpha}\right) - r\left(\frac{1}{\tan\alpha} - \frac{gl}{{u_0}^2\sin\alpha}\right) - \left(\frac{gl^2}{2{u_0}^2} + \frac{d}{\sin\alpha}\right) \qquad (7.4)$$

If the stock level and the trajectory is known at the moment when the dump is charged, the intersection gives the impact point of the particle stream. This intersection may be solved mathematically to give the radial coordinate of the initial apex of the heap to be formed.

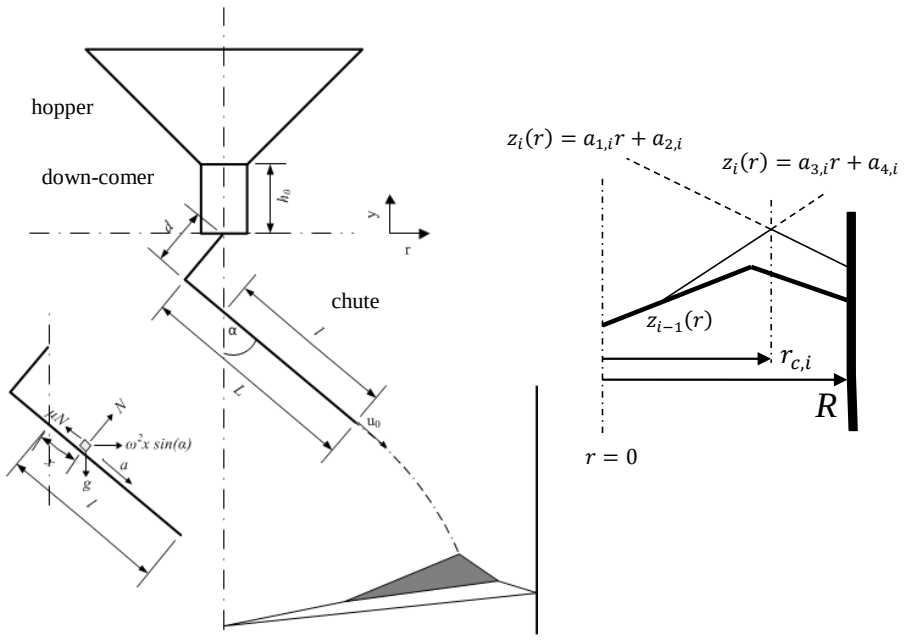

Figure 40: Left: Schematic diagram of the burden distribution model with an inset of force balance of the particle at a point on the chute. Right: Charged layer with a crest at $r = r_{c,i}$. The burden surface before charging is depicted by the thick solid line.

The upper surface of the vertical cross-section of the burden ($z_i(r)$) of a charged dump (here numbered i) is assumed to be composed of two linear segments (cf. right part of Figure 40) given by

$$z_i(r) = \begin{cases} a_{1,i}r + a_{2,i} & if\ r \geq r_{c,i} \\ a_{3,i}r + a_{4,i} & if\ r < r_{c,i} \end{cases} \tag{7.5}$$

where $r_{c,i}$ is the radial coordinate of the crest, which should satisfy eq. 7.4. The slope of the line segments $a_{1,i}$ and $a_{3,i}$ are defined according to the material properties and the position of charging. $a_{2,i}$ and $a_{4,i}$ are determined to satisfy continuity at the crest ($a_{1,i}r_{c,i} + a_{2,i} = a_{3,i}r_{c,i} + a_{4,i}$) and the volume balance. The volume of the i th dump is given by

$$V_i = m_i/\rho_i \tag{7.6}$$

where m is the mass and ρ is the bulk density of the material. Assuming rotational symmetry and the absence of a mixed layer, the physical volume of the dump should be equal to the computed volume

$$V_i = \int_0^{2\pi}\int_0^{R} (z_i(r) - z_{i-1}(r))r\ dr\ d\theta = 2\pi \int_0^{R} (z_i(r) - z_{i-1}(r))r\ dr \tag{7.7}$$

where $z_i(r)$ and $z_{i-1}(r)$ are the equations for the burden surface after and before the ith dump. Taking the location of the computed crest of the dump as the starting point, the algorithm detects the intersection between the lines of eq. 7.5 and the previous burden surface. In case the charged dump extends to the furnace center or the wall, the conditions have to be handled accordingly.

A bell-less top charging system allows charging of thinner layers compared to a bell-top charging system. This results in some computational challenges which need to be handled properly for robustness of the mathematical model. Figure 41 describes one such special case that requires special attention during the determination of the layer surface to avoid sudden changes in the volumes while solving the problem numerically. V_{dump} is the volume of the present dump to be charged on the burden surface. The subfigure (a) shows the burden surfaces formed at different apex heights, *h*, while the (c) schematically presents the volume of the formed burden surfaces at each of those apex heights. The model bears the task of finding an apex height for which the volume of the layer formed equals V_{dump}. In the depicted case this is not possible, because there is an abrupt change in the layer volume for a differential change in apex height, caused by the ridge of the bed. To avoid this problem, a break point is added where the slope of the surface of the layer is changed to be greater than the slope of the lower layer, as indicated in the subfigure (b) of Figure 41. This addition makes the change in volume gradual, as shown in (d), so a computationally valid solution is achieved.

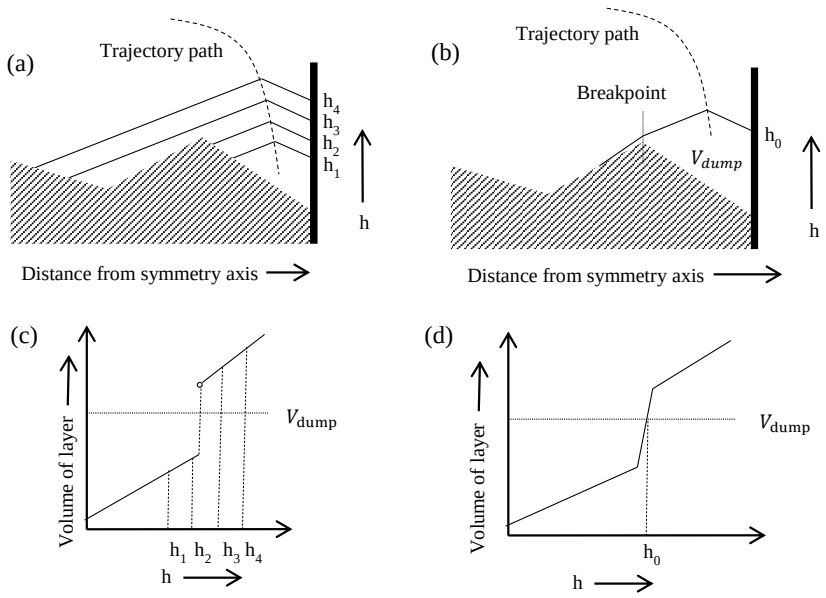

Figure 41: Schematic of layer formation and calculated volume of the charged layer. (a, c): Original formulation leading to infeasible solution, as the volume of the dump (V_{dump}) cannot be satisfied. (b, d): Modified approach, where segment extending over the apex is truncated by locally increasing the repose angle at the apex, making the volume of the layer on the burden surface continuous with the apex height h.

7.2.2 Burden Descent Model

The burden descent model moves the layers downwards computationally between the successive dumps. It is based on the assumption that the material bulk density and other physical properties remain constant as the layers slowly descend through the shaft. The model takes into account the adjustments required for an increase in the diameter of the shaft. In the first version of the model discussed in Paper I, the coke collapse phenomenon is neglected, but subsequently a correction for the collapse is added in Paper IV (described in Sec. 7.7).

As discussed in Sec. 6.4, the particles in the present model are assumed to maintain their relative distance from the symmetry axis. Figure 42 presents a schematic description of the descent philosophy: Points 1-7 in the upper part of the figure represent a series of points on the base surface which supports the layer running through points a-e that exists at this vertical level at time $t = t_0$. The points 3'-5' and b'-d' are points on the layer surface and the base, lying on the path-lines passing through points

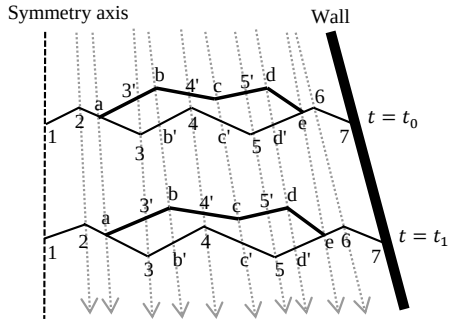

Figure 42 Burden descent procedure. The height of a layer at every point where its limiting surfaces show a discontinuous derivative is considered to preserve the shape and volume of the layer.

3-5 and b-d respectively. At a later time, $t = t_1$, the layer descends to a level illustrated in the lower part of the figure. In this model, the points 1-7, 3'-5', a-e, b'-d' are assumed to always maintain their relative position with respect to the symmetry axis and the wall, so they lie on the same path-line.

Each of the points on the burden surface indicated above can be represented in two dimensions by (r_n, z_n), where r_n is the radial distance from the symmetry axis and z_n is vertical level of the point, for n = 1, 2,…, a, b, … and n' are the corresponding points as described earlier. These points are referred to as bending points and the layer is defined by joining these points using lines which are assumed to remain straight during the descent. However, the layer may be deformed at the bending point, in order to maintain the relative radial distances. This results in the relation

$$\left(\frac{r_n}{R_n}\right)_{t=t_0} = \left(\frac{r_n}{R_n}\right)_{t=t_1} \tag{7.8}$$

$$\left(\frac{r_{n'}}{R_{n'}}\right)_{t=t_0} = \left(\frac{r_{n'}}{R_{n'}}\right)_{t=t_1} \tag{7.9}$$

where R_n is the distance of the wall from the symmetry axis at z_n. The height of the layer at a particular relative radius is defined as

$$h_n = \sqrt{(z_n - z_{n'})^2 + (r_n - r_{n'})^2} \tag{7.10}$$

In the present model the deformation of the layer during its descent is assumed to be uniform, i.e., the ratio between the layer heights at the bending points remains constant during the descent

$$(h_1 : h_2 : \ldots : h_n)_{t=t_0} = (h_1 : h_2 : \ldots : h_n)_{t=t_1} \tag{7.11}$$

Since the formation of mixed layers is neglected, the layer volumes at time t_0 and t_1 should be equal

$$(V)_{t=t_0} = (V)_{t=t_1} \tag{7.12}$$

The points on the descended layer at time t_1 are determined numerically using the above equations.

In the overall calculations, the lowest layer descends with a given velocity distribution, and the remaining layers descend one after the other until the uppermost layer has descended. As the vertical level of the uppermost burden surface at the radial coordinate for the set point has descended below a given value, a new layer is charged and the descent procedure is repeated.

7.2.3 Validation and Use

The burden distribution model was validated using small scale burden distribution experiments. The left part of Figure 43 presents the profiles from an experiment and the distribution predicted by the mathematical model. The right hand part of the figure shows the corresponding ore-to-coke ratios. The

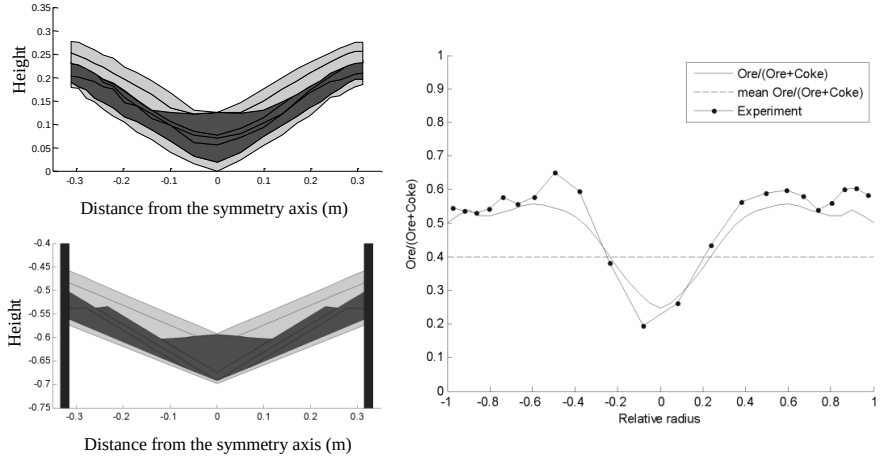

Figure 43: Results from a charging program. Left: Profiles measured in the experimental setup (top) and results from mathematical model (bottom), where ore and coke are represented by light and dark layers, respectively. Vertical coordinates are different due to different reference points. Right: Corresponding O/(O+C) distributions.

results are quite comparable which demonstrates that the model can be used to predict the burden distribution of a blast furnace fairly accurately.

The model was also used to predict the burden distribution in a real blast furnace for an actual charging program which was fairly complicated with more than 120 rings of ore and coke (Figure 44). The gas temperature profile measured on top of the furnace corresponds to the ore-to-coke distribution: The radial regions with higher ore fraction have lower gas temperature and vice-versa. Regions of high coke ratios have higher gas permeability and, therefore, correspond to higher gas temperatures. Thus, the gas temperature and the ore-to-coke distribution correlate negatively with each other.

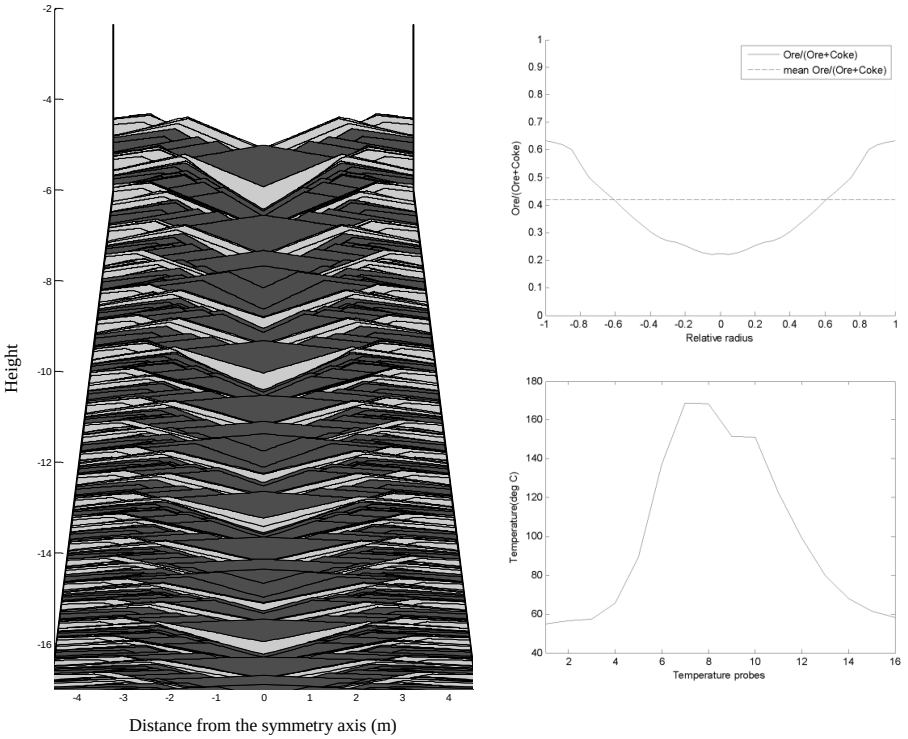

Figure 44: Results for an actual blast furnace. Left: Simulated burden distribution for real furnace, where ore and coke are represented by light and dark layers, respectively. Right: Simulated O/(O+C) distribution (top) and temperature profile from the above-burden probe (bottom)

7.3 Gas flow model (Paper II)

A gas flow model is needed to predict the effect of the burden distribution on the gas flow distribution. Usually the gas flow distribution in a blast furnace is calculated by solving the pressure and gas velocity at 2D or 3D grid points using CFD solvers, but such solvers require a substantial computation time and solution of partial differential equations. Therefore, a relatively simplified approach was taken to obtain a fast solution avoiding the need for commercial CFD software.

Studies of gas flow in the blast furnace [86, 102] have shown that the direction of the gas flow above the cohesive zone of is following the general streamlines as shown in Figure 36. Therefore, the gas flow through the stack of the furnace was approximated to occur through a set of independent concentric rings (Figure 45). The solid was assumed to be quasi stationary. Only the upper part of the furnace was

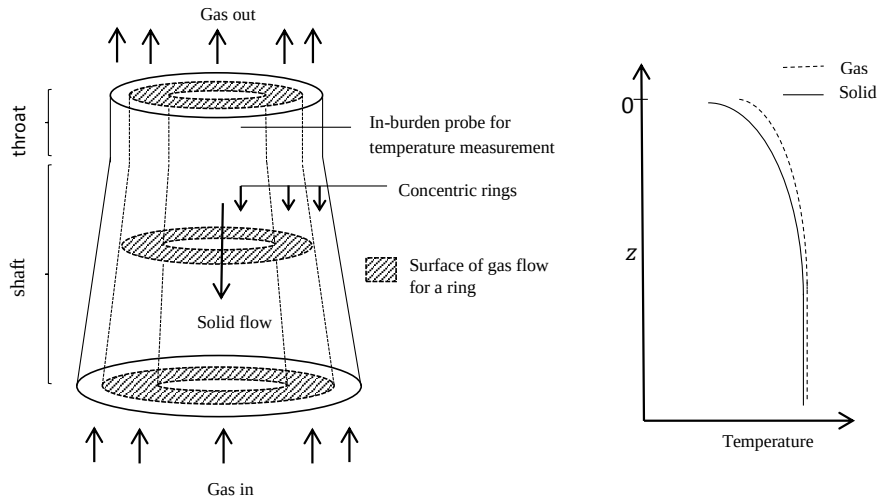

Figure 45: (Left) Schematic diagram of the gas flow model. (Right) Schematic of gas and burden temperatures in a ring.

modelled so the thermal effect of chemical reactions was disregarded and the flows of solid and gas were assumed to be constant in each concentric region. It was assumed that the gas was entering the simulation domain from below through a horizontal plane at the thermal reserve zone temperature (950 °C) and at constant (but unknown) pressure. As the hot gas rises it is cooled by the descending solids, which is implemented by assuming heat sinks at different points which depend on the heat capacity flow of the solids and the temperature difference between the two phases

The heat flow from the gaseous phase to the solid phase is expressed as

$$\frac{\mathrm{d}q_z^i}{\mathrm{d}z} = \left[\varphi^i h_{o,z}^i a_o + \left(1-\varphi^i\right) h_{c,z}^i a_c\right] A_z \left(T_{g,z}^i - T_{s,z}^i\right) \tag{7.13}$$

where φ^i is the volume fraction of ore in cylinder i, a_o and a_c are the specific areas of the ore and coke particles, respectively, while $T_{g,z}^i$ and $T_{s,z}^i$ are the solid and the gas temperatures for cylinder i at height z and the convective heat transfer coefficients are $h_{x,z}^i$ in the ore ($x = o$) and the coke ($x = c$) layer. The furnace is not cylindrical but near the throat it has a constant diameter which starts to increase below the throat. For the ease of calculations, the concentric cylinders are taken to be of equal volumes. Therefore, the cross-sectional areas of each ring at any height (A_z) will be the same for all rings at a particular *z*. The heat transfer coefficient is estimated by

$$h_{x,,z}^i = \frac{\mathrm{Nu}_{x,z}^i \lambda}{d_x} \tag{7.14}$$

where $\mathrm{Nu}_{x,z}^i$ is the Nusselt number for ore and coke given by the modified Ranz equation [103]

$$\mathrm{Nu}_{x,z}^{i} = 2 + 0.6\mathrm{Pr}_{z}^{i\,1/3}\sqrt{9\mathrm{Re}_{x,z}^{i}} \tag{7.15}$$

where the Prandtl number is expressed as

$$Pr_{z}^{i} = \frac{\eta_{z}^{i} c_{g}}{\lambda} \tag{7.16}$$

and λ is the thermal conductivity, η_{z}^{i} the viscosity and c_g the specific heat capacity of the gas. The viscosity of gas was estimated as a function of temperature using the Sutherland formula. [104]

The temperature profiles are solved numerically starting from the given boundary conditions using

$$\frac{\mathrm{d}T_{g,z}^{i}}{\mathrm{d}z} = \frac{1}{\dot{m}_{g}^{i} c_{g}} \frac{\mathrm{d}q_{z}^{i}}{\mathrm{d}z} \tag{7.17}$$

$$\frac{\mathrm{d}T_{s,z}^{i}}{\mathrm{d}z} = \frac{1}{\left(\dot{m}_{o}^{i} c_{o} + \dot{m}_{c}^{i} c_{c}\right)} \frac{\mathrm{d}q_{z}^{i}}{\mathrm{d}z} \tag{7.18}$$

where $\dot{m}_{g}^{i}$ is the mass flow rate of the gas in cylinder i, c_o and c_c are the specific heat capacities of ore and coke, respectively.

The gas pressure drop, due to the resistance of the ore and coke layers is obtained from Ergun's equation [91]

$$\frac{dp_{x,z}^{i}}{dz} = \left(\frac{150}{\mathrm{Re}_{x,z}^{i}} + 1.75\right) \frac{(1-\varepsilon_x)}{{\varepsilon_x}^{3} (\psi_x d_x) \rho_{z}^{i}} \left(\frac{\dot{m}_{g}^{i}}{A_z}\right)^{2} \tag{7.19}$$

$$\frac{dp_{z}^{i}}{dz} = \varphi^{i} \frac{dp_{o,z}^{i}}{dz} + \left(1-\varphi^{i}\right) \frac{dp_{c,z}^{i}}{dz} \tag{7.20}$$

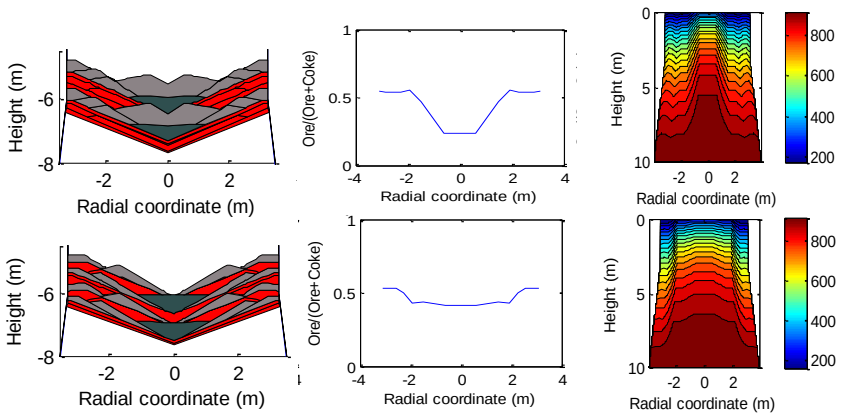

Figure 46: Burden distribution (left) and corresponding ore-to-coke ratio (middle) and the predicted gas temperatures (˚C) (right).

Thus, the effect of the main materials is considered whereas the possible effects of segregation of particles is neglected. The temperature and pressure profiles are solved numerically by discretizing the equations. At the beginning of the calculation a certain gas distribution is assumed for the concentric rings. With the above assumption each of the concentric rings is solved individually using the above equations for variation of pressure, gas and solid temperatures with height. The gas distribution is then iterated until the pressure drop across all the concentric rings is the same. This gives a unique gas distribution, which is considered to be the converged solution.

Figure 46 presents two different burden distributions in a blast furnace, which are evident from the radial distribution of the ore-to-coke ratio. Therefore, the cases result in very different gas distributions as simulated by the gas flow model and presented in the right part of the figure. Figure 47 presents a schematic of how the gas flow model is integrated with the burden distribution and descent models.

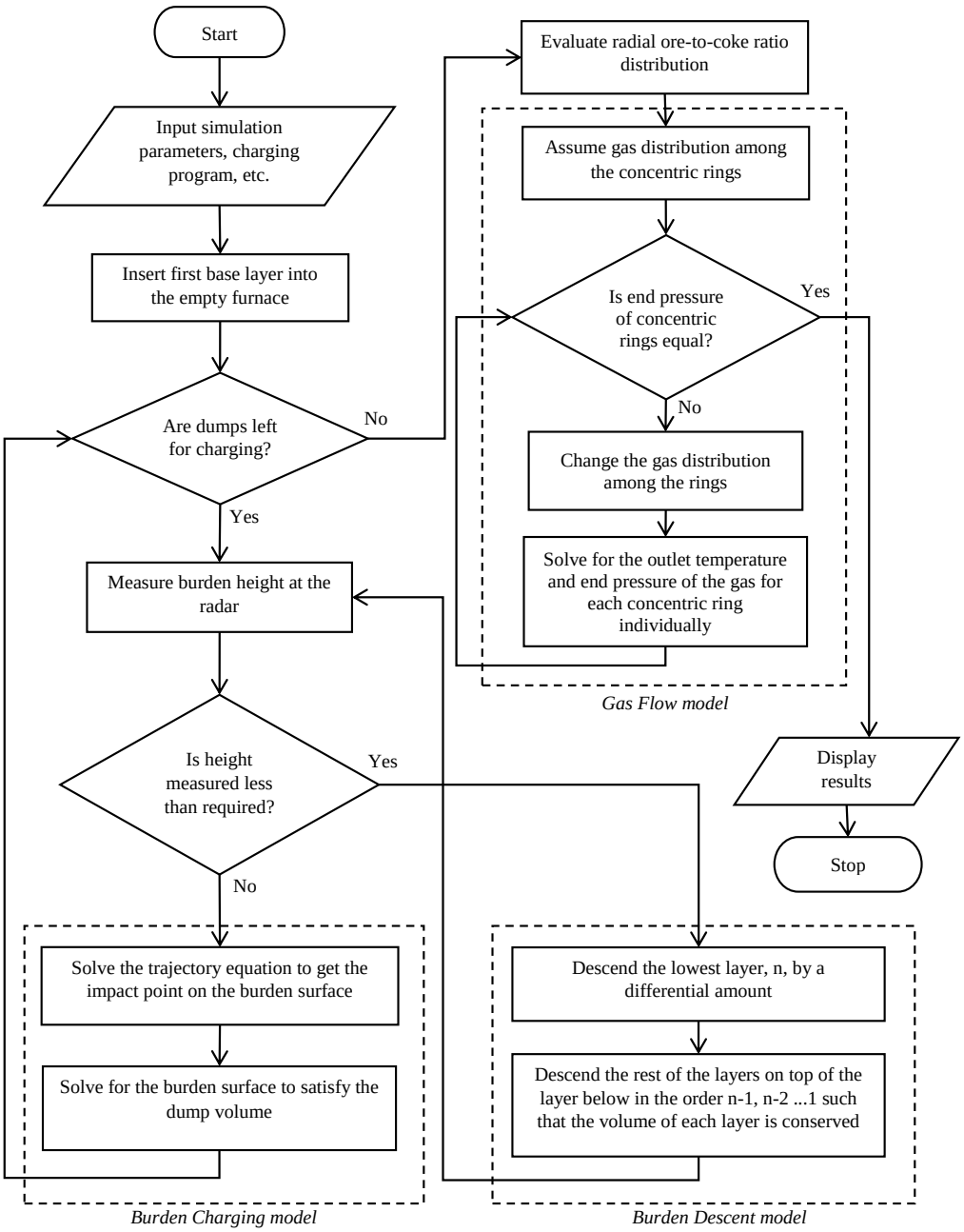

Figure 47: Flowchart describing the burden distribution and the gas flow model

7.4 Optimization using Genetic Algorithm (Paper II)

Blast furnace operators manipulate the charging program partly to target a particular gas flow distribution inside the furnace, which is indirectly sensed through probe information (e.g., gas temperatures and composition along a radius or diagonal). In bell-less top furnaces, the main means of controlling the burden distribution is by changing the chute angle and the order of charges. Mathematical models have been developed for predicting the burden distribution and gas flow inside the furnace, however some strategy was required to systematically search through the innumerable alternative parameter combinations. Such a problem is a non-linear and discontinuous function of the parameters. Genetic Algorithm is very useful for tackling such optimization problems. In this study the classical simple GA as proposed by Holland [42] was used for achieving required temperature profiles at the in-burden probe levels by changing some parameters of a model charging program.

The model charging program consisted of four layers of pellet and coke each and one center coke layer, which could be charged in one of the ways listed in Table 4. The coke dumps could be charged at chute positions of 1-8 whereas the pellet dumps could be charged at positions 4-11 (cf. Table 3). Even for this simplified case, the number of possibilities is enormous; more than 67 million ($4 \times 8^8 = 67{,}108{,}864$) charging programs exist.

Table 4 Different combinations for the charging order and respective bitwise representation. (P: Pellets; C: Coke; CC: Center coke)

Charging order									Bit representation
C	C	C	C	CC	P	P	P	P	00
C	C	P	P	CC	C	C	P	P	01
P	P	C	C	CC	P	P	C	C	10
P	P	P	P	CC	C	C	C	C	11

In the classical GA, the binary chromosome is used to represent a candidate solution. In this case the chromosome was 26 bits long. The first two bits of it indicated the sequence of charging (Table 4) and the subsequent bits in groups of three indicated the chute position for consecutive dumps. The three bits indicate the position 1-8 or 4-11 depending on whether the dump is coke or pellet. Therefore, the chromosome 01 101 011 011 101 111 100 111 110 is interpreted as the charging program $C_6/C_4/P_7/P_9/CC/C_8/C_5/P_{11}/P_{10}$, where C represents coke, P pellet and the subscript indicates the chute position. A set of 50 individual chromosomes were randomly generated to create the initial population, which constituted the parent population. Two-point crossover was carried out between random pairs of parent chromosomes and bitwise mutation was applied to create the offspring population. The crossover and the mutation were carried out with 90% and 4% probability, respectively. The tournament selection

method was used to select the surviving population which acts as the parent for the next generation. This is repeated several times until the population converges to an optimum solution.

Six different targets were specified which represented some typical temperature profiles and the optimization problem was set to minimize the root mean square error (E) between the target ($\hat{T}_i$) and achieved (T_i) temperatures. The achieved temperatures were calculated using the burden distribution and gas flow models (Sec. 7.2 and 7.3)

$$E = \sqrt{\frac{\sum_{i=1}^{N}\left(T_i - \hat{T}_i\right)^2}{N}} \tag{7.21}$$

Figure 48 presents the target and the achieved temperature profiles at the end of the search after 200 generations. There was a very good correspondence of the target and the achieved temperature profile, especially for subplots A-D and F. For subplot E the fit is not so good; a possible reason is that it is difficult to achieve a plateau of high temperature in the center of the furnace with the charging programs available in the present setup.

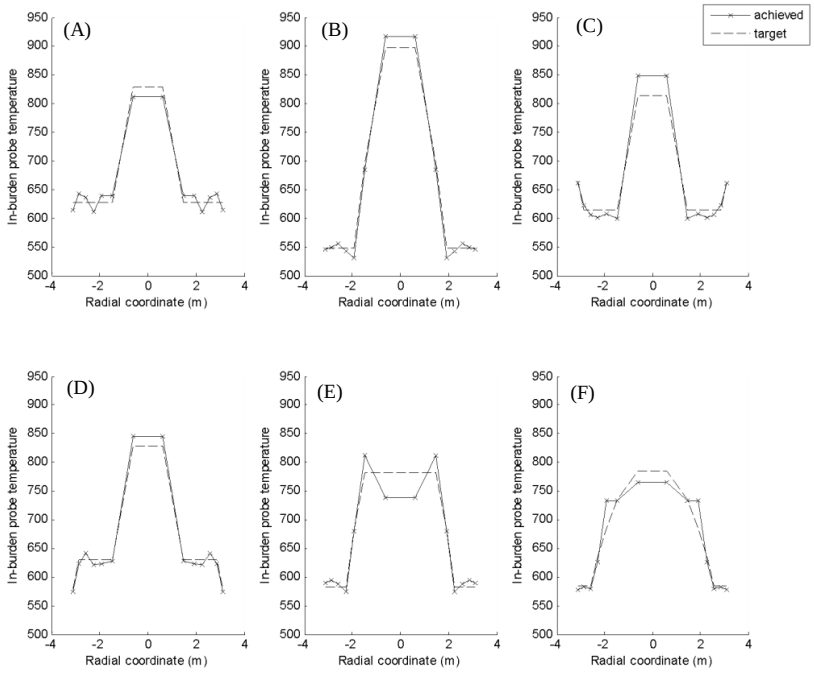

Figure 48 Target (dashed lines) and achieved (solid lines) temperature profiles for the best individuals at the end of the evolution.

The evaluation of one individual chromosome, i.e., the simulation of the burden distribution arising from the charging program, followed by simulation of the gas distribution and calculation of the error compared to the target, took slightly less than half a minute. Therefore, evolution of the individuals for

200 generations, going through a search of about 24000 distinct individuals for each of the targets, took about eight days. This is still acceptable compared to the estimated time of more than 63 years for an exhaustive search among the 67 million possible candidates.

7.5 DEM model of burden distribution (Papers III, IV)

The burden distributions for different charging programs were simulated using EDEM, a commercial software implementing the DEM. The simulation setup (Figure 49) consisted of a channel in which the particles were generated at a rate so that the dump creates a complete ring. The particles fell on the chute, rotating at a constant velocity (0.897 rad/s) around the 'axis' passing through the center of the channel. After that the particle stream slid along the chute and distributed inside the furnace throat. Initially, a conical surface with an angle mimicking the pellet repose angle constituted the lower boundary for the first dump. Later dumps were formed on the layers generated by the previous dumps. DEM simulation is computationally expensive because of a large number of particles and a maximum time step in the order of 10^{-5} s. To reduce the computational burden, a 90˚ section of the throat was simulated which reduced the number of particles considerably. However, this assumption introduced artificial wall effects. Therefore, only a smaller section in the middle, an 'angular slice' of 30° of the simulated region of the throat (Figure 49), was used to report the results. It should also be stressed that because of this setup the particles have very limited space near the center of the furnace, so the results in this region were mostly disregarded in the analysis. Uniform particle size distribution was assumed; therefore size segregation was not considered.

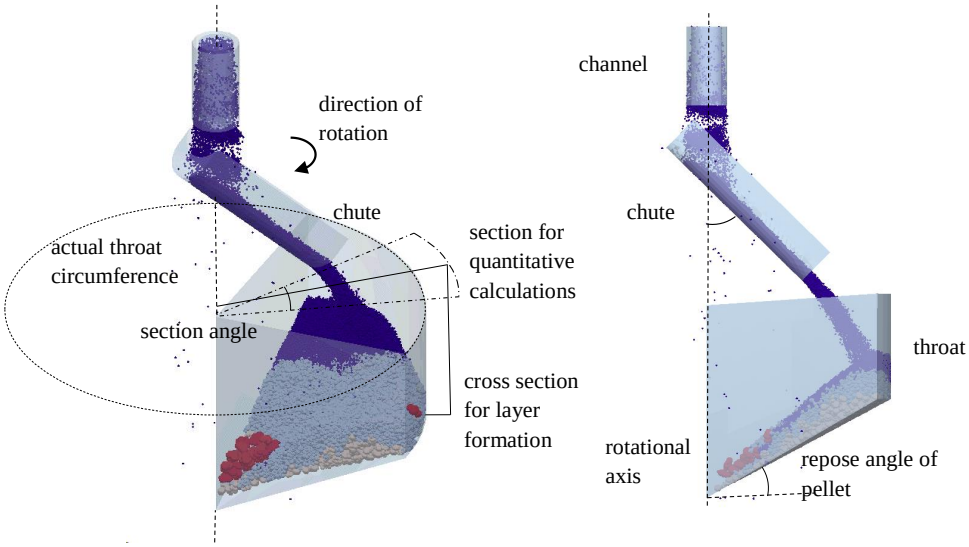

Figure 49: (Left) Isometric view and (right) orthographic view of the simulated charging system.

Results from DEM simulation from a full scale setup and the experimental (small scale) setup were compared. The distances were scaled as 1:10 and the particles were scaled as 1:4 for the two setups. The charging program and some dimensions used for this comparison are shown in Table 5.

Table 5 Charging programs and some dimensions for comparison between experimental scale and full scale simulations.

Material		LC	SC	CC	P	P
Mass (kg)	Experimental scale	3.89	3.89	0.58	16.59	16.59
	Full scale	3888	3888	580	16588	16588
Chute position		6	4	1	10	10
Max. particle diameter (mm)	Experimental scale	12.5	7.5	18	3	3
	Full scale	50	30	72	12	12
Throat diameter (m)	Experimental scale	0.63				
	Full scale	6.3				

Figure 50 shows the cross section for DEM simulations after charging each dump. The subfigures A-E show the result for full scale simulation and subfigures 1-5 are the corresponding simulations using a scaled model. It may be observed that the profiles are quite similar, but yet there are some differences as the particles were not scaled according to the furnace dimension. It accounts for the distinct peak which may be observed in coke dumps in full scale simulation unlike the small scale experiments (subfigures A, B). The effect of pellets pushing the coke dump (subfigures C, D, E and 3, 4, 5) is much more pronounced in full scale because the energy carried by pellet dumps is much higher.

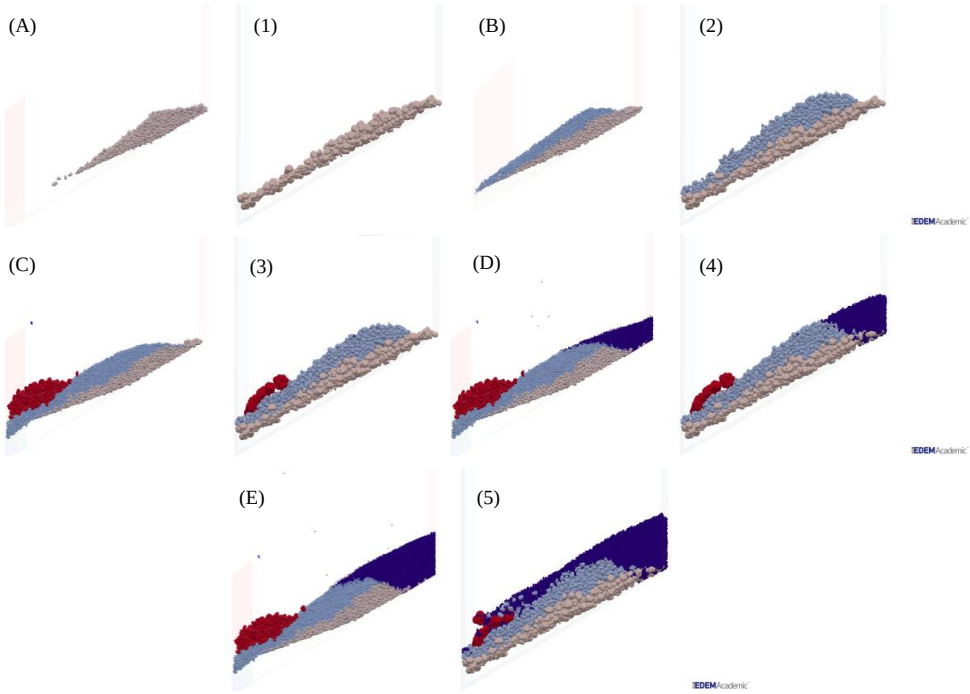

Figure 50: DEM simulation of a charging program in experimental (1-5) and full (A-E)

7.6 Mixed layer formulation (Paper III)

A mixed layer (Figure 51) is a layered volume occupied by multiple particle types, often with a lower voidage than the other parts of the bed. Formation of mixed layer in blast furnaces is important, as some studies have reported it may account for 20-35% of the net pressure drop across the furnace [92]. It is therefore important to understand the formation of the mixed layer in burden distribution calculations. Although the concept of mixed layer is easy to understand, yet a computational definition of the mixed layer is difficult as it requires proper definition of layer boundaries. This can be a challenging task, particularly in three dimensions.

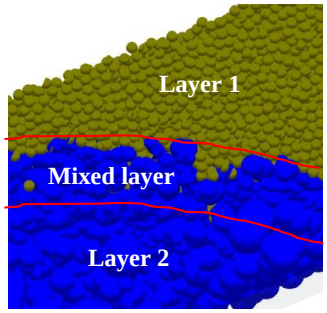

Figure 51: Mixed layer

In this study, the simulation setup is divided into rectilinear grids of control volumes and each of these volumes is assumed to be represented by a single value for the fraction of a particular particle type and for the voidage. The mixed layer is defined as the collection of control volume units that contain more than one particle type or are surrounded by mixed layer volumes. The control volumes surrounded by mixed layer control volumes are also treated as part of the mixed layer to account for the case where a control volume happens to lie in the space between two large particles. It is computationally difficult

and expensive to exactly determine the particles that occupy a certain control volume in DEM. Instead, a stochastic approach was made in this study, where the fraction of the control volume that does not belong to any particle type contributes to the voidage, as outlined below.

The simulation domain is divided into cubic control volumes (v) with side lengths of 5 mm (Δh): each of these control volumes is assumed to be homogeneous. Figure 52 depicts a cross section of the three-dimensional space for easier understanding. The volume fraction of different materials ($k \in$ K) is calculated for each of these individual volumes. A computationally intensive approach would be to geometrically calculate the fraction occupied by the particles. Instead, a Monte-Carlo integration method is utilized here to calculate the share of each particle inside the control volume. For this, 30 pseudorandom points, $j \in$ J, are generated inside each of the cubic control volumes, using the Mersenne Twister algorithm [105]. To deal with non-spherical particles, the calculations consider the particle surfaces, as the irregular particles are enclosed by many spherical surfaces. Since particles with centers appearing in neighboring control volume can also contribute to the current control volume, a skin distance is needed to include or reject such particles. Let I be the set of particle surfaces, i, inside the

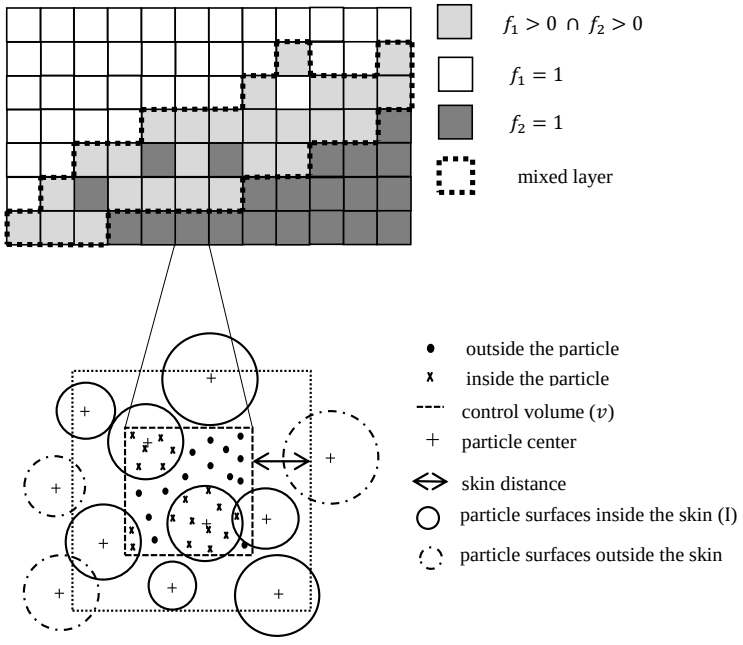

Figure 52: Cross-sectional schematic diagram for calculation of material fraction and mixed layer. The upper part of the figure shows a grid of control volumes and lower part describes an individual control volume with respect to the particle surfaces and the skin distance used for calculation.

region enclosed by another volume whose sides are within the skin distance $r_{\mathrm{I,max}}$ from the control volume sides as described in the lower part of Figure 52, with

$$r_{\mathrm{I,max}} = \max(r_i) \tag{7.22}$$

and where r_i is the radius of the surface i, and $d_{j,i}$ are the distances of the points j from the center of surface i. The material type for each of the i surfaces is denoted by ρ_i . The set of points in the control volume v which belong to a particular material type k is now given by

$$\mathrm{N_k}: \{ j \in J \mid d_{j,i} \leq r_i \mid \rho_i = k \} \tag{7.23}$$

The fraction of material type *k* in the control volume is the ratio of the cardinal numbers of set $\mathrm{N_k}$ and N.

$$f_k = \frac{|\mathrm{N_k}|}{|\mathrm{N}|} \tag{7.24}$$

The voidage of the control volume is, in turn, defined as

$$\varepsilon = 1 - \sum_k f_k \tag{7.25}$$

The simulation setup is enclosed within a mesh ($M \times N \times P$) of such cubic control volumes, $v_{m,n,p}$, where m, n, p indicate the indices of the control volume in the three-dimensional space. Therefore, $m \in [1, M]$, $n \in [1, N]$ and $p \in [1, P]$ and the indices increase along the direction of the axes. The indices of the upper surface of any layer of material k at horizontal indices (m, n) are given by

$$U^k_{m,n} = \max\{ p \mid (f_k)_{m,n,p} \geq 0 \} \tag{7.26}$$

The lower surface control volumes are given by

$$L^k_{m,n} = \min\{ p \mid (f_k)_{m,n,p} \geq 0 \} \tag{7.27}$$

The layer height is therefore

$$h^k_{m,n} = \left(U^k_{m,n} - L^k_{m,n} + 1 \right) \Delta h \tag{7.28}$$

Likewise, for the mixed layer of material k and k', the upper surface ($U^{k,k'}_{m,n}$), lower surface ($L^{k,k'}_{m,n}$) and the layer heights ($h^{k,k'}_{m,n}$) are given by

$$U^{k,k'}_{m,n} = \max\{ p \mid (f_k)_{m,n,p} \geq 0 \cap (f_{k'})_{m,n,p} \geq 0 \} \tag{7.29}$$

$$L^{k,k'}_{m,n} = \min\{ p \mid (f_k)_{m,n,p} \geq 0 \cap (f_{k'})_{m,n,p} \geq 0 \} \tag{7.30}$$

$$h^{k,k'}_{m,n} = \left(U^{k,k'}_{m,n} - L^{k,k'}_{m,n} + 1 \right) \Delta h \tag{7.31}$$

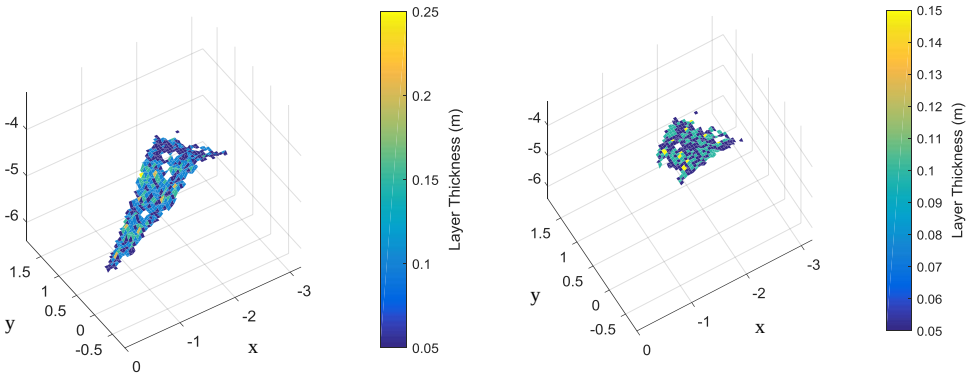

Figure 53: Thickness of the mixed layer composed of two sizes of coke (left), as well as pellet and coke (right).

This formulation may be used to detect the extent and the voidage of mixed layers arising in simulation by DEM, which can give interesting information for gas flow calculations. Figure 53 shows the analysis based on the above formulation for the simulated layers of a full scale DEM simulation based on the materials in Table 5. The first two subfigures show the thicknesses of the mixed layers formed by the two coke sizes (small coke and large coke) and the coke and pellet layers. Each colored point in the figure presents the highest point along the vertical (z) axis of the mixed layer for a particular point on the horizontal (x, y) plane (cf. Eq. 7.29). The color of the point corresponds to the thickness of the mixed layer at the (x, y) coordinate in question. The mixed layer formed by the two different coke sizes is bigger than that by pellet and coke, because the participating particles have greater size.

Figure 54 shows the voidage distribution in a similar manner for each of the individual layers and the mixed layers. Yellow and blue show the regions of high and low voidage respectively. The vertical axis in the figure has been exaggerated for clarity. In general, the coke particles have lower voidage than the pellet particles as the combination of different irregular shapes of the coke particles allows for higher packing than for pellet particles.

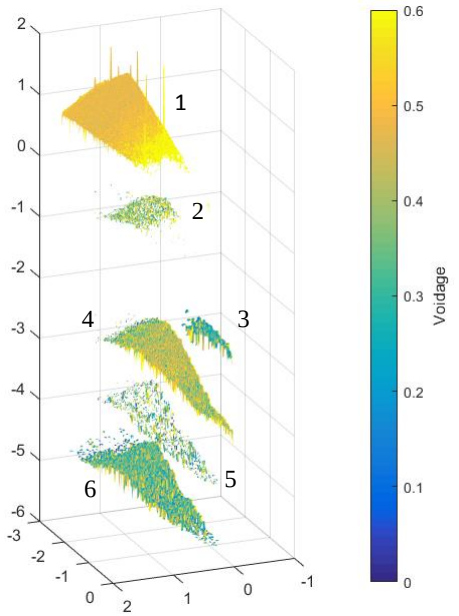

Figure 54: Voidage distribution for all the layers charged into the furnace. (1: Pellet, 2: Mixed, pellet and coke, 3: Center coke, 4: Small coke, 5: Mixed, large coke and small coke, 6: Large coke). The vertical axis is exaggerated for clarity.

7.7 Coke push formulation (Paper IV)

The burden distribution and descent models discussed in Sec. 7.2 did not consider the coke collapse but assumed that the previous layers are stagnant at charging. The model was modified to calculate the stability of a coke layer and to correct the layer structure accordingly using stability theory.

The stability of a slope may be expressed as a ratio between the available shear strength (s) and the shear stress (τ) along a failure plane, referred to as a 'factor of safety'

$$f_s = \frac{s}{\tau} \qquad (7.32)$$

Theoretically the slope is unstable if the factor of safety is less than unity. However, studies have experimentally identified the limit to be closer to 0.8 [53]. The shape of the failure plane may vary but in this study it is assumed to be circular (Figure 55, left), which is a necessary condition for using the 'Ordinary method of slices' [106] for factor of safety calculation. The shear strength is defined in terms of normal stress (σ) on the failure plane. Cohesion between the individual particles is neglected because the particles are large enough. Therefore, the above equation may be written as

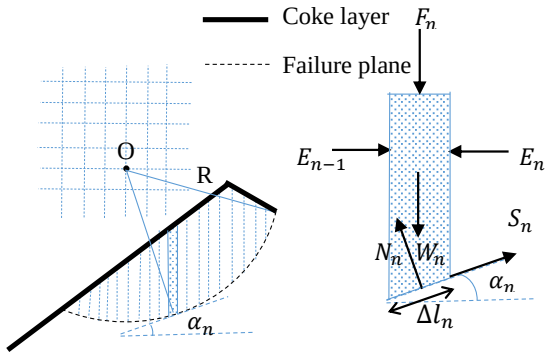

Figure 55: Stability analysis using method of slices. Left: The failure surface and the center of failure surface O. The grid represents the different positions centers of rotation used for evaluating the factor of safety. Right: Forces acting on each slice.

$$f_s = \frac{\sigma \tan \phi}{\tau} \qquad (7.33)$$

where ϕ is the developed friction angle of the material. As per many limit equilibrium methods [106] for calculating the factor of safety for the slip surface, the region above the failure surface is divided into a finite number of thin vertical slices, each with a base length of Δl_n and of unit depth. Figure 55 shows the forces acting on such a slice, n (right panel), located at a particular position on the failure surface (left panel). W_n is the weight and F_n is the external force on the slice, and α_n is the angle made by the tangent on the failure surface to the horizontal. In the ordinary method of slices it is assumed that the inter-slice forces acting in the horizontal direction cancel each other

$$E_{n-1} + E_n = 0 \qquad (7.34)$$

The shear force at the bottom of the slice (S_n) is defined as

$$S_n = \tau_n \Delta l_n \tag{7.35}$$

where τ_n is the shear stress for slice n. Using Eq. (7.33) the above equation may be rewritten as

$$S_n = \frac{\sigma_n \tan \phi}{f_s} \Delta l_n \tag{7.36}$$

where σ_n is the normal stress on slice n, while f_s and ϕ are assumed to remain constant for all the slices.

The normal force on the slip surface is given by

$$N_n = \sigma_n \Delta l_n \tag{7.37}$$

From the free body diagram (Figure 55, right), the normal force may also be expressed as

$$N_n = (W_n + F_n) \cos \alpha_n \tag{7.38}$$

At the critical point of equilibrium, the clockwise and anti-clockwise moments around O, the center of the slip surface, are equal, so

$$\sum_n (W_n + F_n) R \sin \alpha_n = \sum_n S_n R \tag{7.39}$$

where R is the radius of curvature for the slip plane. Substituting the value of S_n from Eq. (7.36) yields

$$\sum_n (W_n + F_n) R \sin \alpha_n = \sum_n \frac{\sigma_n \tan \phi}{f_s} \Delta l_n R \tag{7.40}$$

Using Eqs. (7.37), (7.38) and (7.40) we get

$$\sum_n (W_n + F_n) R \sin \alpha_n = \sum_n \frac{(W_n + F_n) \cos \alpha_n \tan \phi}{\Delta l_n f_s} \Delta l_n R \tag{7.41}$$

Rearranging the equation, an expression for factor of safety is obtained as

$$f_s = \frac{\sum_n (W_n + F_n) \cos \alpha_n \tan \phi}{\sum_n (W_n + F_n) \sin \alpha_n} \tag{7.42}$$

Therefore, when an external force is applied on the heap formed by granular particles the stability of the slope is a function of the magnitude and position of the force acting on the slope, density of the material forming the slope and frictional resistance applied by the material.

This factor of safety is evaluated using different trial points as centers of curvature (intersections of the grid in the left panel of Figure 55). The failure plane is assumed to pass through the intersection of the wall and the layer surface. The minimum value of all the trial points corresponds to the critical factor of safety and it also defines the stability of the layer surface.

During the charging process there are three possibilities. Firstly, the slope does not change significantly due to the incoming stream. Secondly, impact failure may occur when the pellet stream displaces the coke particles but there is no collapse of the layer. Thirdly, gravity failure occurs when the slope is unstable and the particles flow to the center of the furnace, in turn changing the slope of the layer. Each of these three failure modes depend on the shape of the coke layer surface and the radial position of the pellet stream. The factor of safety of a surface depends on these aspects, and a higher factor means a stable slope. In this study the three possibilities are assessed by estimating the factor of safety of a slope: if the value is high enough then the slope is stable, for a medium-level value impact failure is taken to occur, while a low value of the safety factor corresponds to gravity failure. In practice, the impact failure and gravity failure may occur in combination, but this was neglected in the present study to make the model manageable.

Figure 56 shows a schematic diagram of the implementation of the failure modes in the mathematical model. The factor of safety is evaluated for a particular coke surface against a pellet stream entering at a particular position, and it is used to determine if the coke slope needs correction. If the value is lower than a threshold value, impact failure is taken to occur and the coke apex is only moved towards the furnace center but the surface would not collapse. For highly unstable slopes, i.e., very low values of the safety factor, gravity failure is expected where part of the coke layer would break away and slide to the center.

The lower part of Figure 56 schematically illustrates the correction scheme for a coke layer which results in impact failure and gravity failure. To correct the coke layer and to accommodate the failure mechanisms, the apex of the coke layer (r, y) is moved towards the center. The radial displacement, Δr, results in a vertical displacement, Δy, which is calculated from the constraint that the volume of the coke layer before and after the collapse is equal. Thus, no change in voidage is taken to occur and the mixed layer is neglected. In case of impact failure the apex is displaced by a small amount and the corresponding factor of safety for the reconstructed layer is calculated. The factor of safety increases as the apex is moved towards the center. If the factor reaches the limit of stability the displacement is stopped,

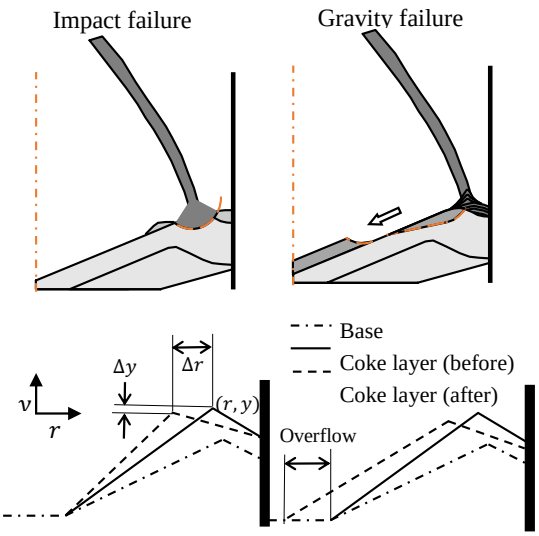

Figure 56: Top: Schematic diagram of two types of coke collapse, impact failure and gravity failure. Bottom: Corresponding implementation in the present mathematical model.

else it is displaced further towards the center and the factor of safety is recalculated. For gravity failure the inner (β_{i}) and outer slopes (β_{o}) of the lines describing the upper surface of the coke layer are decreased because of the collapse, where the decrease depends on the displacement of the apex. The new slopes $\beta_{\mathrm{i,new}}$ and $\beta_{\mathrm{o,new}}$ are given by

$$\beta_{\mathrm{i,new}} = k_{\mathrm{i}} \Delta r \, \beta_{\mathrm{i}} \tag{7.43}$$

$$\beta_{\mathrm{o,new}} = k_{\mathrm{o}} \Delta r \, \beta_{\mathrm{o}} \tag{7.44}$$

where k_{i} and k_{o} are factors determined empirically and they depend on the dimensions of the furnace. As the slopes of the lines are known and are less than the original slope, the layer overflows into the center and the extent of overflow would depend on the degree of instability of the initial slope.

Five model charging programs consisting of a small coke dump, a large coke dump, a center coke dump and two pellet dumps, were studied using DEM and small scale experiments. When the pellet dump was charged over the coke layer, one of the charging programs showed impact failure and another program showed gravity failure whereas, the rest were not affected. This theory was used to predict the occurrence of the collapse and the layer structure after it had collapsed. The model showed good correspondence with the DEM simulations and successfully predicted the collapse. The experiments and the results are detailed in Paper IV.

This method may be utilized to study how prone a particular layer of a charging program is to collapse. Figure 57 shows the mathematical simulation of a complicated charging program based on the conditions in a real furnace with about 20 layers of pellets and coke at various charging positions, repeated over a number of times. In general, it may be observed from the mathematical simulation that the charging program creates two contiguous regions of coke (C1 and C2, consisting of grey and olive layers in the figure) with pellet (P1 and P2, red) regions in between them. One of the coke regions, C1, has an overall slope which is steeper near the furnace center, while the other coke region, C2, has a less steep surface because of a smaller coke dump near the furnace center. Therefore it can be reasoned that the C1 is more prone to failure than C2. In this example, after charging each coke dump, the factor of safety of the layer was calculated if the subsequent dump was pellet. The layers which are prone to collapse are

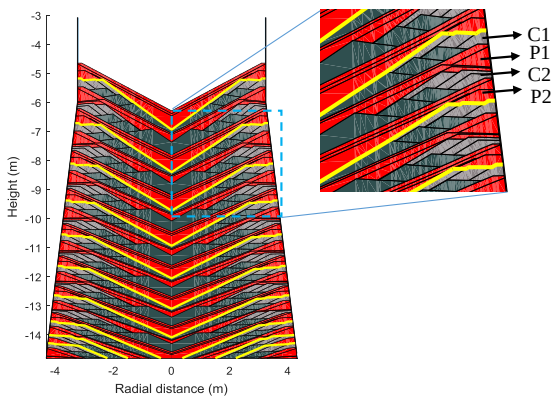

Figure 57: Simulation for a complicated burden distribution program. The slopes which are prone to collapse are marked in yellow. Inset magnifies a portion of the simulation.

marked in yellow in the figure. Thus, the coke collapse theory can help in identifying such regions and also guide the operators in designing more stable programs.

Currently, the outlined procedure can only change the results of the burden distribution model to account for a coke collapse in a limited number of dumps. In the future, the model should be implemented to automatically adjust the burden distribution for layers showing coke collapse.

8. Conclusions

The efficiency of a blast furnace depends largely on the gas flow pattern inside it, as the gas phase is central in the reduction reactions and in the heat transfer. The bed in a blast furnace consists of layers of materials with different physical properties, including density, voidage, particle size and shape. Therefore, controlling the burden distribution is the primary method for achieving a proper gas flow in the furnace and practically the only means of directly controlling the radial distribution of variables in the process. Thus, it is crucial for the furnace operator to understand the effect of the charging program on the formation, shape and thickness of the burden layers. Modern charging equipment allows much more precise charging, but this also increases the number of parameters the operator can modify to achieve the required gas flow. This makes burden distribution optimization a complex problem with a huge number of alternatives. Computational tools are therefore needed to help the operators understand the effect of decisions concerning the choice of charging programs.

In this doctoral work a burden distribution model that can give a quick estimation of the layer structure inside the furnace was developed. The model used simple equations and geometric representations of the layers to achieve a fast model which can be run in less than half a minute. Small scale experiments were used to verify the results from the mathematical model, which showed reasonable agreement with the findings from the charging experiments.

The burden distribution model provided the distribution of materials in the furnace, which was used to develop a model simulating the gas and solid temperature in the upper part of the furnace with reasonable simplifications. A genetic algorithm was used to optimize the charging programs to attain a particular gas temperature distribution at the vertical level of an in-burden (below burden) probe. The search was efficient and the algorithm was found to be suitable for discontinuous and non-differentiable problems like the problem at hand.

Particle methods like DEM are much more helpful for understanding the flow of bulk solids than continuum methods. DEM was used in this thesis to gain an understanding of the burden formation behavior for different charging programs. To account for the shape of coke particles a clumped sphere model was used successfully. The simulation results were used to study mixed layers. In scaled simulation the mixed layer was found to have around 12% lower voidage than the layers of individual components. The formulation for calculating the voidage distribution in the furnace would be useful for CFD calculations studying the gas flow in the blast furnace by continuum models.

In charging experiments and the DEM simulations, it was observed that for particular charging programs the coke layer collapsed when heavier pellets were charged at higher charging positions. Therefore, a model based on slope stability analysis was developed to classify the extent of coke collapse and a scheme was outlined of how to change the layer structure to make it stable to the loading

condition. The simulations and the experimental results demonstrated that the scheme could capture the behavior fairly well. A collapse may be avoided by charging the coke closer to the furnace center or at least splitting the coke dump to partially charge it further off from the wall.

9. Future prospects

In this doctoral work, a mathematical model was developed for rapid simulation of burden distribution in the blast furnace. A simplified gas distribution model was also developed using the results from the burden distribution model. A genetic algorithm was used to find the right combination of charging parameters for a target gas distribution. Additionally, DEM models and charging experiments were applied to gain a deeper understanding of the phenomena at charging. Even though these models and experiments have provided insight into the central factors and phenomena involved in the distribution of the burden in the blast furnace, further work is still required.

The mathematical models may be optimized further to reduce the calculation overhead times. The coke collapse model developed in this thesis should be fully integrated with the burden distribution model to make the layer correction procedure robust enough for handling complicated charging programs. A graphical user interface for the mathematical model has already been built to facilitate its interactive use in steel industry, but in the future the model should also be connected to the industrial database to allow for real time calculations.

The gas flow model has to be improved significantly to allow crossflows and accurate treatment of the solid flow. The data from the gas flow model could then be matched with the temperature probe readings from the plant, possibly in online use. This would make it possible to predict internal variables, such as the cohesive zone shape in the furnace, which would give extremely useful information to the blast furnace operator.

DEM provides a means of gaining insight into the flow behavior of particles in the furnace, but the heavy computational burden still makes it impossible to simulate the whole furnace with true particle sizes. However, as the computation technology improves, especially with the advent of GPU (Graphics Processing Unit) accelerated computing, the computation times will decrease and it is likely that full-scale simulation will be feasible in the near future. Meanwhile, there are several other phenomena related to the behavior of bulk solids which need to be understood further, especially in context of blast furnaces. The effect of particle shapes and particle size distribution on the burden distribution should be studied further. The conditions inside the blast furnace are also particularly interesting, because the gas flow affects the distribution of smaller particles (fines). Coupled CFD-DEM simulation can help in understanding such phenomena in detail.

Finally, more research would be needed to fully understand the physical and chemical processes in the blast furnace. Better understanding of the coupling of different processes can be used to improve the efficiency of blast furnace charging. This will help in reducing the coke rates and thereby reduce the production cost and carbon footprint of ironmaking process, paving the way to a more sustainable future.

References

[1] D. R. Lide, Ed., *CRC Handbook of Chemistry and Physics.* New York: CRC Press, 1996.

[2] A. Ghosh and A. Chatterjee, *Iron Making and Steelmaking: Theory and Practice.* PHI Learning Pvt. Ltd., 2008.

[3] (2016, Feb 16). *Annual iron production archive.* Available: http://www.worldsteel.org/statistics/statistics-archive/iron-archive.html.

[4] A. Carpenter, "CO2 abatement in the iron and steel industry," *IEA Clean Coal Centre,* 2012.

[5] J. De Beer, "Future technologies for energy-efficient iron and steel making," in *Potential for Industrial Energy-Efficiency Improvement in the Long Term*Anonymous Springer, 2000, pp. 93-166.

[6] J. G. Peacey and W. G. (. G. Davenport, *The Iron Blast Furnace : Theory and Practice.* Oxford ; New York : Pergamon Press, 1979.

[7] A. Rist and N. Meysson, "A Dual Graphic Representation of the Blast Furnace Mass and Heat Balances," *Journal of Metals,* vol. 19, pp. 50-59, 1967.

[8] I. Muchi, "Mathematical Model of Blast Furnace," *Transactions of the Iron and Steel Institute of Japan,* vol. 7, pp. 223-&, 1967.

[9] A. Kilpinen, "An on-line model for estimating the melting zone in a blast furnace," *Chemical Engineering Science,* vol. 43, pp. 1813-1818, 1988.

[10] N. K. Nath, "Simulation of gas flow in blast furnace for different burden distribution and cohesive zone shape," *Materials and Manufacturing Processes,* vol. 17, pp. 671-681, 2002.

[11] X. F. Dong, D. Pinson, S. J. Zhang, A. B. Yu and P. Zulli, "Gas-powder flow in blast furnace with different shapes of cohesive zone," *Applied Mathematical Modelling,* vol. 30, pp. 1293-1309, 11, 2006.

[12] M. Hatano and K. Kurita, "A Mathematical Model of Blast Furnace with Radial Distribution of Gas Flow, Heat Transfer and Reactions Considered," *Transactions of the Iron and Steel Institute of Japan,* vol. 22, pp. 448-456, 1982.

[13] Z. Zhou, H. Zhu, A. Yu, B. Wright, D. Pinson and P. Zulli, "Discrete particle simulation of solid flow in a model blast furnace," *ISIJ International,* vol. 45, pp. 1828-1837, 2005.

[14] J. A. de Castro, H. Nogami and J. Yagi, "Three-dimensional Multiphase Mathematical Modeling of the Blast Furnace Based on the Multifluid Model." *ISIJ International,* vol. 42, pp. 44-52, 2002.

[15] A. Adema, *DEM-CFD Modelling of the Ironmaking Blast Furnace.* TU Delft, Delft University of Technology, 2014.

[16] H. Saxén and F. Pettersson, "Nonlinear prediction of the hot metal silicon content in the blast furnace," *ISIJ International,* vol. 47, pp. 1732-1737, 2007.

[17] A. Agarwal, U. Tewary, F. Pettersson, S. Das, H. Saxén and N. Chakraborti, "Analysing blast furnace data using evolutionary neural network and multiobjective genetic algorithms," *Ironmaking & Steelmaking,* vol. 37, pp. 353-359, 2010.

[18] A. Biswas, *Principles of Blast Furnace Ironmaking : Theory and Practice.* Brisbane Australia: Cootha, 1981.

[19] J. J. Poveromo, "Burden distribution fundamentals," vol. 22-23, 1995-1996.

[20] H. Takahashi, H. Kawai, M. Kobayashi and T. Fukui, "Two dimensional cold model study on unstable solid descending motion and control in blast furnace operation with low reducing agent rate," *ISIJ International,* vol. 45, pp. 1386-1395, 2005.

[21] A. Murao, Y. Kashihara, N. Oyama, M. Sato, S. Watakabe, K. Yamamoto and Y. Fukumoto, "Development of control techniques for mixing small coke at bell-less top blast furnace." *ISIJ International,* vol. 55, pp. 1172-1180, 2015.

[22] P. K. Gupta, A. S. Rao, V. R. Sekhar, M. Ranjan and T. K. Naha, "Burden distribution control and its optimisation under high pellet operation," *Ironmaking & Steelmaking,* vol. 37, pp. 235-239, 2010.

[23] B. D. Pandey and U. S. Yadav, "Blast furnace performance as influenced by burden distribution," *Ironmaking & Steelmaking,* vol. 26, pp. 187-192, 1999.

[24] M. Riddle and P. Whitfield, "Design and operation of a Gimbal Top distribution system for ironmaking plants," *Revue De Métallurgie,* vol. 104, pp. 113-119, 2007.

[25] B. Boranbaev, Y. Glazer, V. Vakulin and A. Sirkar, "Bell-less rotary charging unit–A perfect burden loading technology," *Metallurgist,* vol. 53, pp. 395-403, 2009.

[26] R. Timmer, J. Droog, G. Flierman and A. Steeghs, "Radial gas distribution in the blast furnace top," *Steel Research,* vol. 68, pp. 47-53, 1997.

[27] S. Nag, A. Gupta, S. Paul, D. J. Gavel and B. Aich, "Prediction of Heap Shape in Blast Furnace Burden Distribution," *ISIJ International,* vol. 54, pp. 1517-1520, 2014.

[28] M. Naito, K. Takeda and Y. Matsui, "Ironmaking technology for the last 100 years: deployment to advanced technologies from introduction of technological know-how, and evolution to next-generation process," *ISIJ International,* vol. 55, pp. 7-35, 2015.

[29] H. P. Zhu, Z. Y. Zhou, R. Y. Yang and A. B. Yu, "Discrete particle simulation of particulate systems: A review of major applications and findings," *Chemical Engineering Science,* vol. 63, pp. 5728-5770, 12/1, 2008.

[30] DEM Solutions Ltd., "EDEM," vol. 2.3-2.7, 2010-2015.

[31] DEM Solutions Ltd., "EDEM 2.3 user guide," 2010.

[32] H. Hertz, "On the contact of elastic solids," *Journal Für Die Reine Und Angewandte Mathematik,* vol. 92, pp. 156-171, 1881.

[33] P. A. Cundall and O. D. Strack, "A discrete numerical model for granular assemblies," *Geotechnique,* vol. 29, pp. 47-65, 1979.

[34] M. Kremmer and J. F. Favier, "A method for representing boundaries in discrete element modelling—part II: Kinematics," *International Journal for Numerical Methods in Engineering,* vol. 51, pp. 1423-1436, 2001.

[35] S. Ueda, S. Natsui, Z. Fan, H. Nogami, R. Soda, J. Kano, R. Inoue and T. Ariyama, "Influences of physical properties of particle in discrete element method on descending phenomena and stress distribution in blast furnace," *ISIJ International,* vol. 50, pp. 981-986, 2010.

[36] G. Defendi, A. Baltazar, P. F. Nogueira, A. G. Cornejo and D. S. Nasato, "Blast furnace charging simulation using EDEM," in *Proceedings EDEM Conference 2011,* Edinburgh, Scotland, 2011, pp. 291-311.

[37] Y. Yu and H. Saxén, "Flow of Pellet and Coke Particles in and from a Fixed Chute," *Industrial & Engineering Chemistry Research,* vol. 51, pp. 7383-7397, 2012.

[38] H. Matuttis and J. Chen, *Understanding the Discrete Element Method: Simulation of Non-Spherical Particles for Granular and Multi-Body Systems.* John Wiley & Sons, 2014.

[39] T. Pöschel and T. Schwager, *Computational Granular Dynamics: Models and Algorithms.* Springer Science & Business Media, 2005.

[40] K. Deb, *Multi-Objective Optimization using Evolutionary Algorithms.* John Wiley & Sons, 2001.

[41] T. Mitra, H. Saxén and N. Chakraborti, "Evolutionary algorithms in ironmaking applications," in *Evolutionary Computation: Techniques and Applications*, A. M. Gujrathi and B. V. Babu, Eds. Ontario: Apple Academic Press, 2016, .

[42] J. H. Holland, *Adaptation in Natural and Artificial Systems: An Introductory Analysis with Applications to Biology, Control, and Artificial Intelligence.* U Michigan Press, 1975.

[43] V. R. Radhakrishnan and K. M. Ram, "Mathematical model for predictive control of the bell-less top charging system of a blast furnace," *Journal of Process Control,* vol. 11, pp. 565-586, 2001.

[44] R. Balevičius, R. Kačianauskas, Z. Mróz and I. Sielamowicz, "Analysis and DEM simulation of granular material flow patterns in hopper models of different shapes," *Advanced Powder Technology,* vol. 22, pp. 226-235, 3, 2011.

[45] A. W. Jenike, "Gravity flow of bulk solids," *Bulletin no.108, Utah State University,* 1961.

[46] S. Jung and W. Chung, "Improvement of Gas Flow through Analyzing Discharge Behavior in the Bunker Used in Blast Furnace." *ISIJ International,* vol. 41, pp. 1324-1330, 2001.

[47] Y. Yu and H. Saxén, "Experimental and DEM study of segregation of ternary size particles in a blast furnace top bunker model," *Chemical Engineering Science,* vol. 65, pp. 5237-5250, 2010.

[48] P. A. Langston, U. Tüzün and D. M. Heyes, "Discrete element simulation of granular flow in 2D and 3D hoppers: Dependence of discharge rate and wall stress on particle interactions," *Chemical Engineering Science,* vol. 50, pp. 967-987, 3, 1995.

[49] P. W. Cleary and M. L. Sawley, "DEM modelling of industrial granular flows: 3D case studies and the effect of particle shape on hopper discharge," *Applied Mathematical Modelling,* vol. 26, pp. 89-111, 2, 2002.

[50] A. Anand, J. S. Curtis, C. R. Wassgren, B. C. Hancock and W. R. Ketterhagen, "Predicting discharge dynamics from a rectangular hopper using the discrete element method (DEM)," *Chemical Engineering Science,* vol. 63, pp. 5821-5830, 12, 2008.

[51] S. Watakabe, K. Takeda, H. Nishimura, S. Goto, N. Nishimura, T. Uchida and M. Kiguchi, "Development of high ratio coke mixed charging technique to the blast furnace," *ISIJ International,* vol. 46, pp. 513-522, 2006.

[52] Y. Kashihara, Y. Morikawa, T. Sato, N. Ishiwata and M. Sato, "Development of Charging Technique for Controlling Mixed Coke Distribution in Ore Layer," *ISIJ International,* vol. 55, pp. 1165-1171, 2015.

[53] S. Nag and V. Koranne, "Development of material trajectory simulation model for blast furnace compact bell-less top," *Ironmaking & Steelmaking,* vol. 36, pp. 371-378, 2009.

[54] T. Mitra and H. Saxén, "Model for fast evaluation of charging programs in the blast furnace," *Metallurgical and Materials Transactions B,* vol. 45, pp. 2382-2394, 2014.

[55] J. Park, H. Jung, M. Jo, H. Oh and J. Han, "Mathematical modeling of the burden distribution in the blast furnace shaft," *Metals and Materials International,* vol. 17, pp. 485-496, 2011.

[56] Z. Teng, S. Cheng, P. Du and X. Guo, "Mathematical model of burden distribution for the bell-less top of a blast furnace," *International Journal of Minerals, Metallurgy, and Materials,* vol. 20, pp. 620-626, 2013.

[57] Y. Yu and H. Saxén, "Analysis of rapid flow of particles down and from an inclined chute using small scale experiments and discrete element simulation," *Ironmaking & Steelmaking,* vol. 38, pp. 432-441, 2011.

[58] H. Mio, S. Komatsuki, M. Akashi, A. Shimosaka, Y. Shirakawa, J. Hidaka, M. Kadowaki, S. Matsuzaki and K. Kunitomo, "Validation of particle size segregation of sintered ore during flowing through laboratory-scale chute by discrete element method," *ISIJ International,* vol. 48, pp. 1696-1703, 2008.

[59] J. Zhang, J. Qiu, H. Guo, S. Ren, H. Sun, G. Wang and Z. Gao, "Simulation of particle flow in a bell-less type charging system of a blast furnace using the discrete element method," *Particuology,* vol. 16, pp. 167-177, 2014.

[60] H. Mio, S. Komatsuki, M. Akashi, A. Shimosaka, Y. Shirakawa, J. Hidaka, M. Kadowaki, S. Matsuzaki and K. Kunitomo, "Effect of chute angle on charging behavior of sintered ore particles at bell-less type charging system of blast furnace by discrete element method," *ISIJ International,* vol. 49, pp. 479-486, 2009.

[61] J. Jimenez, J. Mochon and J. S. d. Ayala, "Mathematical model of gas flow distribution in a scale model of a blast furnace shaft," *ISIJ International,* vol. 44, pp. 518-526, 2004.

[62] H. Saxén, M. Nikus and J. Hinnelä, "Burden distribution estimation in the blast furnace from stockrod and probe signals," *Steel Research,* vol. 69, 1998.

[63] H. Saxén and J. Hinnelä, "Model for burden distribution tracking in the blast furnace," *Mineral Processing and Extractive Metallurgy Review,* vol. 25, pp. 1, 2004.

[64] Q. Zhu, C. Lu, Y. Yin and X. Chen, "Burden distribution calculation of bell-less top of blast furnace based on multi-radar data," *Journal of Iron and Steel Research, International,* vol. 20, pp. 33-37, 2013.

[65] S. Matsuzaki, "Estimation of stack profile of burden at peripheral zone of blast furnace top," *ISIJ International,* vol. 43, pp. 620-629, 2003.

[66] D. Fu, Y. Chen and C. Q. Zhou, "Mathematical modeling of blast furnace burden distribution with non-uniform descending speed," *Applied Mathematical Modelling,* vol. 39, pp. 7554-7567, 12, 2015.

[67] P. Y. Shi, D. Fu, P. Zhou and C. Q. Zhou, "Evaluation of stock profile models for burden distribution in blast furnace," *Ironmaking and Steelmaking,* 2015.

[68] J. Jimenez, J. Mochon, A. Formoso and J. S. d. Ayala, "Burden distribution analysis by digital image processing in a scale model of a blast furnace shaft," *ISIJ International,* vol. 40, pp. 114-120, 2000.

[69] J. Xu, S. Wu, M. Kou, L. Zhang and X. Yu, "Circumferential burden distribution behaviors at bell-less top blast furnace with parallel type hoppers," *Applied Mathematical Modelling,* vol. 35, pp. 1439-1455, 2011.

[70] Y. Kajiwara, T. Jimbo and T. Sakai, "Development of a simulation model for burden distribution at blast furnace top." *Transactions of the Iron and Steel Institute of Japan,* vol. 23, pp. 1045-1052, 1983.

[71] T. Mitra and H. Saxén, "Discrete element simulation of charging and mixed layer formation in the ironmaking blast furnace," *Computational Particle Mechanics*, pp. 1-15, 2015.

[72] C. K. Ho, S. M. Wu, H. P. Zhu, A. B. Yu and S. T. Tsai, "Experimental and numerical investigations of gouge formation related to blast furnace burden distribution," *Minerals Engineering*, vol. 22, pp. 986-994, 2009.

[73] S. M. Wu, H. P. Zhu, A. B. Yu and P. Zulli, "Numerical investigation of crater phenomena in a particle stream impact onto a granular bed," *Granular Matter*, vol. 9, pp. 7-17, 2007.

[74] S. Nag, S. Basu and A. B. Yu, "A static approach towards coke collapse modelling in blast furnace," *Ironmaking & Steelmaking*, vol. 36, pp. 509-514, 2009.

[75] D. Tsai, C. Lo, J. Jeng and C. Ho, "A study on burden distribution of blast furnace with a bell-less top," *Journal of the Chinese Institute of Engineers*, vol. 11, pp. 199-205, 1988.

[76] S. Wu, C. Fu, C. Liu, X. Jian and M. Kou, "Coke collapse model and collapse profile variation law for bell-less top BF," *Journal of Iron and Steel Research, International*, vol. 18, pp. 8-12, 2011.

[77] H. Nishio and T. Ariyama, "Analysis on formation processes of burden distribution in a blast furnace," *Tetsu-to-Hagane*, vol. 68, pp. 2330-2337, 1982.

[78] M. Ichida, K. Nishihara, K. Tamura, M. Sugata and H. Ono, "Influence of ore/coke distribution on descending and melting behavior of burden in blast furnace." *ISIJ International*, vol. 31, pp. 505-514, 1991.

[79] S. Natsui, S. Ueda, Z. Fan, N. Andersson, J. Kano, R. Inoue and T. Ariyama, "Characteristics of solid flow and stress distribution including asymmetric phenomena in blast furnace analyzed by discrete element method," *ISIJ International*, vol. 50, pp. 207-214, 2010.

[80] Z. Fan, S. Natsui, S. Ueda, T. Yang, J. Kano, R. Inoue and T. Ariyama, "Transient behavior of burden descending and influence of cohesive zone shape on solid flow and stress distribution in blast furnace by discrete element method," *ISIJ International*, vol. 50, pp. 946-953, 2010.

[81] Z. Fan, S. Igarashi, S. Natsui, S. Ueda, T. Yang, R. Inoue and T. Ariyama, "Influence of blast furnace inner volume on solid flow and stress distribution by three dimensional discrete element method," *ISIJ International*, vol. 50, pp. 1406-1412, 2010.

[82] Y. Yu, A. Westerlund, T. Paananen and H. Saxén, "Inter-particle percolation segregation during burden descent in the blast furnace," *ISIJ International,* vol. 51, pp. 1050-1056, 2011.

[83] Y. Yu and H. Saxén, "Effect of DEM parameters on the simulated inter-particle percolation of pellets into coke during burden descent in the blast furnace," *ISIJ International,* vol. 52, pp. 788-796, 2012.

[84] J. Park, U. Baek, K. Jang, H. Oh and J. Han, "Development of the burden distribution and gas flow model in the blast furnace shaft," *ISIJ International,* vol. 51, pp. 1617-1623, 2011.

[85] K. Yang, S. Choi, J. Chung and J. Yagi, "Numerical modeling of reaction and flow characteristics in a blast furnace with consideration of layered burden," *ISIJ International,* vol. 50, pp. 972-980, 2010.

[86] D. Fu, Y. Chen, Y. Zhao, J. D'Alessio, K. J. Ferron and C. Q. Zhou, "CFD modeling of multiphase reacting flow in blast furnace shaft with layered burden," *Applied Thermal Engineering,* vol. 66, pp. 298-308, 5, 2014.

[87] X. Dong, A. Yu, S. Chew and P. Zulli, "Modeling of blast furnace with layered cohesive zone," *Metallurgical and Materials Transactions B,* vol. 41, pp. 330-349, 2010.

[88] Y. Shen, T. Shiozawa, P. Austin and A. Yu, "Model study of the effect of bird's nest on transport phenomena in the raceway of an ironmaking blast furnace," *Minerals Engineering,* vol. 63, pp. 91-99, 8, 2014.

[89] J. Szekely and J. Poveromo, "A mathematical and physical representation of the raceway region in the iron blast furnace," *Metallurgical and Materials Transactions B,* vol. 6, pp. 119-130, 1975.

[90] Y. Feng, D. Pinson, A. Yu, S. J. Chew and P. Zulli, "Numerical study of gas-solid flow in the raceway of a blast furnace," *Steel Research International,* vol. 74, pp. 523-530, 2003.

[91] S. Ergun, "Fluid flow through packed columns," *Chemical Engineering Progress,* vol. 48, pp. 89-94, 1952.

[92] M. Guha, S. Nag, P. K. Swamy and R. V. Ramna, "Effect of Interface Resistance on Gas Flow in Blast Furnace," *ISIJ International,* vol. 51, pp. 1795-1799, 2011.

[93] J. Liu, Q. Xue, X. She and J. Wang, "Investigation on interface resistance between alternating layers in the upper of blast furnace," *Powder Technology,* vol. 246, pp. 73-81, 2013.

[94] Z. Qing-tian and C. Shu-sen, "“Redistribution” Effect of Lumpy Zone for Gas Flow in BF," *Journal of Iron and Steel Research, International,* vol. 14, pp. 1-7, 11, 2007.

[95] G. Qing, L. Ma, X. Zhang, J. Zhou and M. Kuwabara, "Numerical investigation of gas flow through blast furnace shaft with designed layered structure of ore and coke burdens," *Ironmaking & Steelmaking,* vol. 37, pp. 546-552, 2010.

[96] T. Mitra and H. Saxén, "Evolution of charging programs for achieving required gas temperature profile in a blast furnace," *Materials and Manufacturing Processes,* vol. 30, pp. 474-487, 2015.

[97] Y. Shen, B. Guo, S. Chew, P. Austin and A. Yu, "Three-dimensional modeling of flow and thermochemical behavior in a blast furnace," *Metallurgical and Materials Transactions B,* vol. 46, pp. 432-448, 2015.

[98] S. Natsui, H. Takai, R. Nashimoto, T. Kikuchi and R. O. Suzuki, "Model study of the effect of particles structure on the heat and mass transfer through the packed bed in ironmaking blast furnace," *International Journal of Heat and Mass Transfer,* vol. 91, pp. 1176-1186, DEC, 2015.

[99] J. Q. An, K. Peng, W. H. Cao and M. Wu, "Modeling of High Temperature Gas Flow 3D Distribution in BF Throat Based on the Computational Fluid Dynamics," *Journal of Advanced Computational Intelligence and Intelligent Informatics,* vol. 19, pp. 269-276, MAR, 2015.

[100] S. K. Kodukula and H. Saxén, "Model of radial distributions in the upper part of the blast furnace shaft," *Steel Research International,* vol. 78, pp. 843-848, 2007.

[101] A. A. Kjellman, "Design, construction and testing of a pilot blast furnace bell-less top model," *Åbo Akademi University,* 2009.

[102] S. Natsui, H. Nogami, S. Ueda, J. Kano, R. Inoue and T. Ariyama, "Simultaneous three-dimensional analysis of gas-solid flow in blast furnace by combining discrete element method and computational fluid dynamics," *ISIJ International,* vol. 51, pp. 41-50, 2011.

[103] J. Yagi and I. Muchi, "Improved mathematical model for estimating process variables in blast furnace," *Transactions of the Iron and Steel Institute of Japan,* vol. 10, pp. 181-187, 1970.

[104] A. J. Smits and J. Dussauge, *Turbulent Shear Layers in Supersonic Flow*. Springer Science & Business Media, 2006.

[105] M. Matsumoto and T. Nishimura, "Mersenne twister: a 623-dimensionally equidistributed uniform pseudo-random number generator," *ACM Transactions on Modeling and Computer Simulation (TOMACS)*, vol. 8, pp. 3-30, 1998.

[106] Anonymous "Slope stability," US Army Corps of Engineers, Tech. Rep. EM 1110-2-1902, 2003.

ISBN 978-952-12-3419-4
Painosalama Oy
Turku/Åbo, Finland 2016